Radial and Non-Radial Oscillations of Protoneutron Stars with Hyperonic Composition

Prashant Thakur •,1,2,* Adamu Issifu •,3,† Ishfaq Ahmad Rather •,4,‡ Y. Lim •,2,§ and Tobias Frederico •,3,¶

1 Department of Physics, BITS-Pilani, K. K. Birla Goa Campus, 403726 Goa, India,

2 Department of Physics, Yonsei University, Seoul, 03722, South Korea

3 Departamento de Física e Laboratório de Computação Científica Avançada e Modelamento (Lab-CCAM),

Instituto Tecnológico de Aeronáutica, DCTA, 12228-900, São José dos Campos, SP, Brazil

4 Institut für Theoretische Physik, Goethe Universität,

Max-von-Laue-Str. 1, D-60438 Frankfurt am Main, Germany

This paper explores radial and non-radial oscillations of protoneutron stars (PNSs) as they evolve from hot, neutrino-rich states through deleptonization to cold, catalyzed configurations. The equation of state (EoS) is modeled using a density-dependent relativistic mean-field framework, with stellar evolution guided by entropy and lepton fraction. Both nucleonic and hyperonic matter compositions are considered. Non-radial f- and p_1 -mode oscillations are computed using the Cowling approximation and full general relativity. The presence of trapped neutrinos increases the Cowling approximation error for f-modes, which decreases during deleptonization and rises again in the cold phase. In contrast, p_1 -modes exhibit the highest errors during intermediate evolutionary stages due to complex pressure and density gradients at this stage. The emergence of hyperons modestly increases the oscillation frequencies in both f- and p_1 -modes. Additionally, existing universal relations for the f-mode frequency and damping time lack model independence for PNSs, motivating the proposition of a more robust and realistic relation in this work. In particular, our universal relation with moment of inertia shows excellent agreement across all evolutionary stages, highlighting $\tilde{\eta}$ as an effective temperature-sensitive scaling for model-independent asteroseismology. The radial oscillation properties for a $1.4 M_{\odot}$ PNS across different evolutionary stages using nucleonic and hyperonic EoSs are also investigated. Our analysis reveals that both the displacement (ξ) and pressure perturbation (η) profiles are sensitive to thermal conditions, composition, and stellar compactness. Hyperonic stars exhibit higher oscillation frequencies, altered node structures, and enhanced pressure perturbation amplitudes due to the softening of the EoS. The frequency separation $\Delta \nu_n$ and the fundamental mode frequency ν_0 show clear distinctions between nucleonic and hyperonic models, with hyperons inducing nonlinear behaviors and enhanced sensitivity to core structure. These signatures provide valuable diagnostic tools to probe the internal composition and evolution of PNS and constrain the dense matter EoS through asteroseismology.

I. INTRODUCTION

The study of core-collapse supernova (CCSNe) is a crucial topic in nuclear physics, as it is one of the few phenomena where all four fundamental forces of nature interact, shaping the dynamics of stellar collapse and explosion. Gravity drives the collapse when a massive star exhausts its nuclear fuel, the electromagnetic force governs interactions between charged particles, the weak nuclear force facilitates neutrino interactions, and the strong nuclear force dictates the behavior of nuclear matter at extreme densities [1, 2]. Aside from that, CCSNe serve as a suitable phenomenon for probing the emission of light particles with masses $\lesssim 100 \text{ MeV} [3, 4]$. Additionally, the observation of the neutrino burst from neutron star (NS) 1987A [5, 6] marked a turning point in particle physics, leading to further constraints on neutrino properties.

The implosion of the massive star leads to the formation of a PNS when the core contracts and heats up. This collapse releases a vast amount of energy, causing an explosion and resulting in the creation of a hot PNS [7–10]. Over time, the PNS undergoes processes such as neutrino emission, deleptonization, thermal radiation, and neutrino diffusion, which cause it to cool and contract, ultimately forming a cold, catalyzed NS [11]. To study the thermodynamic evolution of PNSs, the EoS is essential, as it relates pressure, energy density, and temperature, providing insight into the composition and properties of matter within the PNS [12–17].

In this work, we use the EoS initially published in [14], which has been extensively applied in studies on quark core formation in PNSs [15] and the impact of mirror dark matter on PNS evolution [18]. Our primary objective is to investigate the radial and non-radial oscillations of PNSs during their evolutionary stages and to examine how the emergence of hyperons influences these oscillations. This analysis provides deeper insights into the structure, stability, and composition of PNSs as they evolve. A key advantage of our approach is that radial and non-radial oscillations offer complementary perspectives. Radial oscillations primarily probe the stability, expansion, and contraction of PNSs, but they do not produce direct observational signatures in gravitational waves. In [19], the authors analyzed the radial oscillations of PNSs and determined that the oscillation frequency is lower in neutrino-trapped matter. They also observed

^{*} p20190072@goa.bits-pilani.ac.in

[†] ai@academico.ufpb.br

[‡] rather@astro.uni-frankfurt.de

[§] ylim@yonsei.ac.kr

[¶] tobias@ita.br

a rapid decline in the fundamental frequencies near the maximum mass. Further studies on radial oscillations of PNSs are fairly limited because of the complex physical processes in PNS and can be found in [20–22].

In contrast, non-radial oscillations provide crucial insights into the internal composition of PNSs, including the role of exotic matter such as hyperons. Additionally, they serve as valuable probes of gravitational wave signals, offering rich astrophysical information. Interested readers may refer to Refs. [23–29], and the references therein, for further details on the f- and p_1 -mode oscillations. However, studying non-radial oscillations presents significant mathematical and computational challenges. By investigating both radial and non-radial modes together, we obtain a more comprehensive understanding of how temperature and the presence of hyperons influence the properties and dynamics of PNSs. More importantly, in the non-radial case, we compare full general relativity (GR) calculations with the Cowling approximation for the first time in the study of PNSs' evolution with exotic baryon composition. The present work extends the analysis of Ref. [24], which focused on non-radial oscillations in PNSs using full GR but did not include neutrino effects or hyperonic matter.

These two approaches differ in key ways: the full GR method considers both fluid perturbations, which peak near the stellar surface, and metric perturbations, which peak at the stellar center. In contrast, the Cowling approximation neglects metric perturbations, introducing small errors, particularly in massive stars, where strong fluid perturbations dominate [26]. Our goal is to quantify the deviation of the Cowling approximation from the full GR approach throughout stellar evolution and to assess the role of neutrinos, temperature, and hyperons in this deviation. Furthermore, [30] demonstrated that as PNSs evolve, changes in the frequencies and damping times of non-radial oscillations significantly impact their structural properties and gravitational wave emission.

The work is organized as follows: In Section II, we present the microphysics governing the evolution of the PNSs. Section III briefly describes the formalism for radial and non-radial oscillation modes. In Section IV, we present the EoS, mass-radius relations, and analyze the f-mode frequency with several subsections discussing the gravitational-wave asteroseismology, highlighting universal relations and the behavior of p-mode frequencies as well as radial profiles, and Gravitational-wave detectability. Finally, we summarize our findings and conclusions in Section V.

II. MICROPHYSICS

The EoS used for hadronic interactions is based on quantum hadrodynamics (QHD) [31], which describes strong interactions between hadrons mediated by massive mesons. The full Lagrangian density for the relativistic mean-field approximation model [32] is given by:

$$\mathcal{L}_{\text{RMF}} = \mathcal{L}_H + \mathcal{L}_{\text{m}} + \mathcal{L}_{\text{l}}, \tag{1}$$

where \mathcal{L}_H , \mathcal{L}_m , and \mathcal{L}_l represent the Lagrangian densities for the baryon octet, the meson fields, and the leptons, respectively. Explicitly:

$$\mathcal{L}_{H} = \sum_{b \in H} \bar{\psi}_{b} \Big[i \gamma^{\mu} \partial_{\mu} - \gamma^{0} \big(g_{\omega b} \omega_{0} + g_{\phi b} \phi_{0} + g_{\rho b} I_{3b} \rho_{03} \big) - \Big(m_{b} - g_{\sigma b} \sigma_{0} \Big) \Big] \psi_{b}, \tag{2}$$

$$\mathcal{L}_{\rm m} = -\frac{1}{2}m_{\sigma}^2\sigma_0^2 + \frac{1}{2}m_{\omega}^2\omega_0^2 + \frac{1}{2}m_{\phi}^2\phi_0^2 + \frac{1}{2}m_{\rho}^2\rho_{03}^2, \quad (3)$$

$$\mathcal{L}_{l} = \sum_{l} \bar{\psi}_{l} \left(i \gamma^{\mu} \partial_{\mu} - m_{l} \right) \psi_{l}. \tag{4}$$

Here, ψ_b is the baryonic Dirac field with the subscript b representing the individual baryons present, $i = \sigma$, ω , ϕ and ρ are the meson fields with ω and ϕ being the vectorisoscalar meson (where ϕ has a hidden strangeness), σ is a scalar meson and ρ is a vector-isovector mesons while the subscript '0' represents the mean-field approximation presentation. The corresponding masses of the mesons are given by; m_i with their values provided in Table I, $I_{3b} = \pm 1/2$ is the isospin projection and ψ_l is the free lepton fields with the subscript 'l' representing the different lepton species in the system. The baryon octet and the lepton species have a degeneracy of two, except in a situation where neutrinos are trapped in the stellar matter; at this stage, we consider electron neutrinos (ν_e) with a degeneracy of one, in consistency with supernova physics [8]. At the neutrino-trapped regime, we neglect the presence of muons in our analysis since their presence becomes only relevant after all the neutrinos have escaped from the stellar core [1]. Additionally, in the neutrinotransparent stage, when all the neutrinos have escaped from the stellar core, we consider the presence of electrons (e) and muons (μ) in the stellar matter, while tau leptons are considered too heavy to be present [7, 16].

Moreover, we consider the presence of hyperons in the stellar core at each stage of the star's evolution, mediated by the ϕ meson with mass $m_{\phi}=1019.45$ MeV. The presence of hyperons in the stellar core is theoretically predicted as a result of energy minimization in high-density environments, where the increasing degeneracy pressure of nucleons makes hyperon formation energetically favorable. This process is governed by the Pauli exclusion principle, which dictates the behavior of fermionic particles. The emergence of hyperons introduces additional degrees of freedom, reducing the net energy of the system and, consequently, softening the EoS. This phenomenon, commonly referred to as the hyperon puzzle, has been extensively discussed in the literature [32, 33].

We employ the density-dependent coupling adjusted by the DDME2 parameterization [34] represented by:

$$g_{iN}(n_B) = g_{iN}(n_0)a_i \frac{1 + b_i(\eta + d_i)^2}{1 + c_i(\eta + d_i)^2},$$
 (5)

with $i = \sigma, \omega, \phi$ and

$$g_{\rho N}(n_B) = g_{\rho N}(n_0) \exp\left[-a_{\rho}(\eta - 1)\right]. \tag{6}$$

Here, $\eta = n_B/n_0$, where $n_0 = 0.152$ fm⁻³ is the baryon saturation density under this parameterization and n_B is

TABLE I. DDME2 parameters for nucleonic matter in this work.

meson(i)	$m_i({ m MeV})$	a_i	b_i	c_i	d_i	$g_{iN}(n_0)$
σ	550	1.3881	1.0943	1.7057	0.4421	10.5396
ω	783	1.3892	0.9240	1.4620	0.4775	13.0189
ho	763	0.5647			_	7.3672

the baryon density. The model parameters (a_i, b_i, c_i) and d_i) are determined through fitting to experimental bulk nuclear matter properties around n_0 . Other nuclear properties for this parameterization include the binding energy, compressibility modulus, symmetry energy, and its density slope, given by B/A = -16.4 MeV, $K_0 = 251.9 \text{ MeV}$, J = 32.3 MeV, and L = 51.3 MeV, respectively [34–37]. To incorporate hyperons within this framework, extensive work has been done to extend the couplings using various methods [38, 39]. These approaches aim to obtain a massive hyperonic star with a maximum mass consistent with the observed NS mass threshold of $2 M_{\odot}$. For this paper, we adopt the coupling constraints determined in [40], which uses SU(3) and SU(6) symmetry arguments to extend the nucleon-meson couplings to include hyperons and Δ -resonances in a unified framework. The advantage of this choice of coupling is that it leads to massive hyperonic stars within the $2 M_{\odot}$ threshold. The corresponding parameters for hyperons are listed in Table II, represented as the ratio of the nucleon-meson couplings in the form $\chi_{ib} = g_{ib}/g_{iN}.$

II.1. Conditions Relevant for PNS Evolution

The corresponding EoS is determined by solving the components of the energy-momentum tensor of the \mathcal{L}_{RMF} in Eq. (1). To construct stable and potentially observable stars, we enforce charge neutrality and β -equilibrium conditions in calculating the EoS. Detailed formulations and applications of the EoS can be found in [14–16, 32]. Rather than repeating the derivation of these EoSs, we highlight only the key relations relevant to this work. The Helmholtz free energy of the system is given by: $\mathcal{F} = \varepsilon_t - Ts$, with ε_t as the total energy of the system, s as the entropy density, and T as the temperature distribution of the system. The expression that connects s, T, ε_t , P_t (total pressure), μ_i (the chemical potential of the individual particles represented by j) and n_i (the number density of the individual particles) derived from \mathcal{F} is given by,

$$sT = \varepsilon_t + P_t - \sum_b \mu_b n_b - \sum_l \mu_l n_l, \tag{7}$$

where the sum; b and l are over all the baryons and leptons, respectively. Applying charge neutrality and β -equilibrium conditions to the above expression, we obtain

$$sT = P_t + \varepsilon_t - n_B \mu_B - \mu_{\nu_o} (n_{\nu_o} + n_e), \tag{8}$$

TABLE II. The ratio of the baryon coupling to the corresponding nucleon coupling for hyperons.

b		$\chi_{\sigma b}$		
Λ		0.646	0	-0.808
Σ^0	1	0.663	0	-0.404
Σ^-, Σ^+				
Ξ^-, Ξ^0	0.571	0.453	0	- 1.01

for the neutrino-trapped regime, where the neutrino number density modifies the resulting equation, and

$$sT = P_t + \varepsilon_t - n_B \mu_B, \tag{9}$$

for the neutrino-transparent regime [15].

To study the evolutionary stages, we divide our analysis into two broad phases: the neutrino-trapped and neutrino-transparent phases. We adopt the quasi-static approximation to study PNS evolution, assuming the star evolves through a sequence of equilibrium states. To simplify the analysis, we impose ad hoc thermodynamic conditions on the stellar configurations. This approach provides a reasonable description of the PNS structure, simplifies calculations, and facilitates comparison with certain simulation results [7–10]. The outcomes are examined in four distinct snapshots. The first stage corresponds to the birth of a PNS in the core of a massive star that has exhausted its nuclear fuel. In this phase, the core becomes opaque to neutrinos, which temporarily sustains thermal pressure and influences the PNS's evolution. Meanwhile, the stalled shock wave must be revived to trigger a successful supernova explosion. We simulate this phase by fixing the lepton fraction at $Y_l = 0.4$ and define the entropy per baryon as $s_B = s/n_B = 1$. The second stage is the deleptonization phase, occurring approximately 0.5 to 1 second after the explosion. During this period, the PNS rapidly loses neutrinos, leading to a reduction in the Y_l . In the model framework, we fix $Y_l = 0.2$ and $s_B = 2$ for this stage.

The third stage occurs after nearly all neutrinos have escaped from the stellar core, approximately 50s after the explosion, marking the transition to the cooling phase. At this point, the matter has reached its peak temperature and begins to cool down. In the model framework we set $Y_{\nu_e} = 0$ and $s_B = 2$. The final stage occurs after the star has cooled over several decades to centuries ($\sim 50-100$ years or more), forming cold and catalyzed NS. The EoS is constrained by both experimental and observational data to ensure that, at the end of the star's evolution, its structure remains consistent with key astrophysical constraints. These constraints include the GW170817 event [41, 42] and recent measurements from the NICER X-ray observatory, which provides mass and radius measurements for pulsars such as PSR J0740+6620 [43, 44] and PSR J0030+0451 [45, 46].

III. OSCILLATION MODES

III.1. Non-Radial

In the full GR framework, non-radial oscillations of NS are analyzed by introducing small perturbations to the static background spacetime metric. These perturbations lead to oscillation modes whose complex frequencies encode both the actual oscillation (through the real part) and the damping due to gravitational wave emission (through the imaginary part). In this approach, the complete set of Einstein's field equations is solved by considering gravitational waves as perturbations to the static metric of a non-rotating star.

In contrast, the Cowling approximation simplifies the problem by neglecting the perturbations in the gravitational field and focusing solely on the fluid perturbations within the star. By disregarding the back-reaction on the gravitational potential, the Cowling approximation reduces the computational complexity of the problem. However, this simplification comes at the cost of slightly less accurate frequency estimates, since it does not fully capture the dynamic interplay between the metric and the fluid, which is intrinsic to the complete GR treatment [25– 27]. In the present study, we are using both formalisms to make a comparison of the f- and p_1 -mode frequencies for different stages of NS evolution. For a detailed derivation and the underlying equations, see Ref. [47]. Since buoyancy plays a negligible role in these modes, it is common to approximate the adiabatic and equilibrium sound speeds as equal, i.e., $c_s^2 \approx c_e^2$, in this formalism. This simplifies the analysis by effectively setting the Brunt-Väisälä frequency to zero, thereby excluding buoyancy-driven qmodes. More details can be found in Ref. [48]. This approximation is particularly justified in the quasi-static treatment of PNSs, where entropy and lepton number profiles are fixed. Similar simplifications have been used in earlier works employing both full GR [24, 49] and the Cowling approximation [50].

III.2. Radial

In a spherically symmetric system with radial motion, the metric function becomes explicitly time-dependent, allowing one to employ the Einstein field equations to analyze the radial oscillation characteristics of a static equilibrium configuration [51]. In this framework, the radial displacement, denoted by Δr , and the pressure perturbation, ΔP , are introduced to quantify the star's response to small perturbations. By defining the dimensionless variables $\xi = \Delta r/r$ and $\eta = \Delta P/P$, the problem reduces to solving a set of perturbed differential equations. For a full description of the Radial oscillations, see Refs. [52, 53].

Although the detailed derivation involves these coupled equations, the essential idea is to integrate them under appropriate boundary conditions. At the center of the star, regularity conditions are imposed (e.g., $\eta = -3\gamma \xi$),

while at the stellar surface the requirement that the Lagrangian pressure perturbation vanishes selects discrete eigenvalues of ω^2 . These eigenvalues correspond to the natural modes of radial oscillation, ordered by the number of nodes in the radial eigenfunctions. In particular, the fundamental mode (with no nodes) is critical for assessing the stability of the star, as real eigenfrequencies indicate a stable configuration, whereas any imaginary component would signal instability.

The oscillation frequencies are commonly expressed in kHz, scaled by a dimensionless constant and a characteristic frequency $\omega_0 \equiv \sqrt{M/R^3}$, where M and R represent the mass and radius of the star, respectively. Numerical methods such as the shooting method are typically employed to integrate the equations from the center to the surface, ensuring that all boundary conditions are met and yielding a discrete spectrum of radial eigenfrequencies.

The analysis of radial oscillations for PNSs presented herein assumes an isentropic EoS throughout the star's evolutionary stages. The radial oscillations are mathematically modeled as infinitesimal adiabatic perturbations of the stellar equilibrium configuration, which fundamentally implies the absence of heat transfer and entropy modification during the oscillatory process. Furthermore, in deriving the isentropic EoS that governs PNS evolution, s_B is fixed, which aligns fundamentally with the assumption of adiabatic perturbations. As a result, this approach eliminates the necessity for thermal correction terms, preserving the computational efficiency of stability and pulsation analyses while maintaining their theoretical integrity. The underlying mathematical framework governing this discussion remains valid and can be found in Ref. [54]. Moreover, this analytical framework extends analogously to non-radial oscillations, as both modalities are predicated on the small adiabatic perturbation assumption and utilize the EoS as a fundamental input parameter.

IV. RESULTS AND ANALYSIS

IV.1. Equation of State and Mass-Radius relations

Figure 1 illustrates the structure of PNSs as determined using the TOV equations [58, 59], showing their evolution from neutrino-rich objects at birth to cold, catalyzed NS at maturity. While PNSs undergo significant thermal and compositional evolution, their structure at any given time can be approximately described by the hydrostatic equilibrium configuration using the TOV framework [7, 10]. The results obtained from this process are then compared with those of observed pulsars, with the corresponding confidence contours shown in the right panel of Figure 1. The full details of the thermodynamic conditions relevant for PNS evolution and how they impact the structure of the star can be found in Refs. [7, 8].

Aside from the leptons, whose composition depends on the star's evolutionary stage, we consider PNSs composed solely of nucleons, as well as those containing both

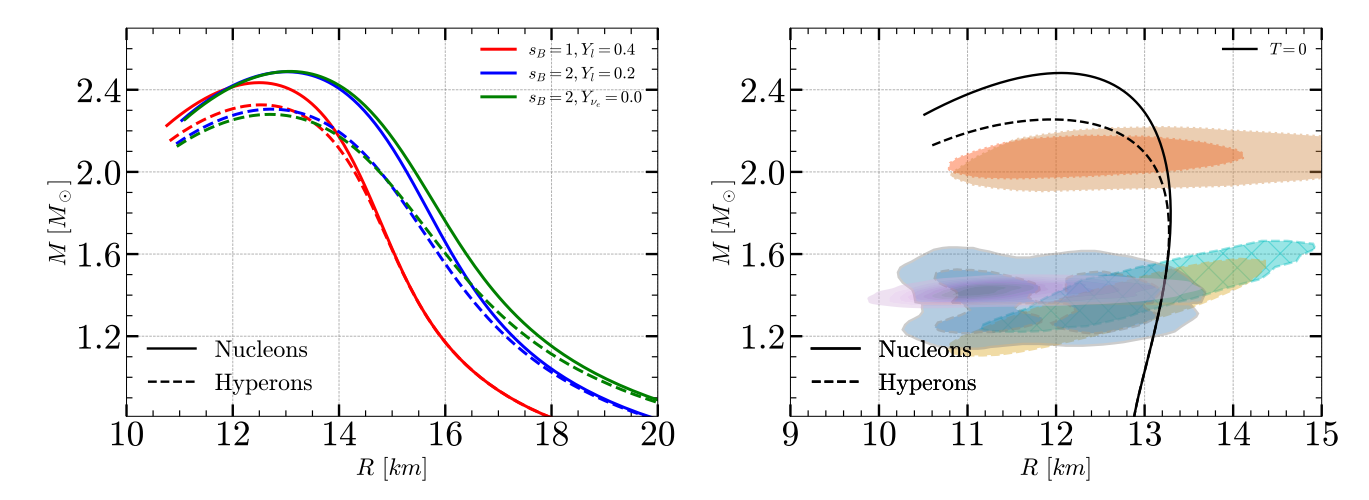


FIG. 1. Right: Total gravitational mass (M) of a cold NS as a function of its radius (R). The steel blue region represents the constraints derived from the binary components of GW170817, highlighting their respective 90% and 50% credible intervals. Additionally, the 1σ (68%) confidence intervals for the 2D mass-radius posterior distributions of the millisecond pulsars PSR J0030+0451 (depicted in cyan and yellow) [46, 55] and PSR J0740+6620 (shown in orange and peru) [44, 56], obtained from NICER X-ray observations, are included. Furthermore, the plot presents the most recent NICER constraints on the mass and radius of PSR J0437-4715 (illustrated in lilac) [57]. Left: Same as right plot, but for a PNS capturing the evolutionary stages of neutrino-trapped, β -equilibrated stellar matter. These stages are characterized by different entropy per baryon (s_B) and lepton fraction (Y_I) , and are compared with a neutrino-transparent star where $s_B = 2$ and $Y_{\nu_e} = 0$.

nucleons and hyperons. In general, we find that the presence of hyperons lowers the star's maximum mass, as expected [33]. This occurs because the onset of hyperons introduces additional degrees of freedom, weakening the pressure support at higher densities. Consequently, the EoS softens, and the star can support less mass against gravitational collapse [15, 16]. From Table III, comparing the maximum masses, we observe that in nucleon-only stellar matter, the neutrino-trapped phase allows the star to sustain about $0.05 M_{\odot}$ more mass from the first to the second phase, with the star expanding due to heating. On the other hand, when hyperons are present, the star's mass decreases from the first to the second stage, even as it expands. In the neutrino-transparent phase—the third and final stage—the star shrinks and becomes more compact, experiencing a slight reduction in mass and a significant decrease in radius for both matter compositions.

Figure 2 shows the temperature distribution in the stellar matter as a function of the baryon density in unit of baryon saturation density. In the first stage, the temperature is lowest when the s_B is minimal and the Y_l is highest. In the second stage, the temperature reaches its peak in the core. In the third stage, where the stellar matter is expected to attain its maximum temperature before cooling, the temperature rises to \sim $3n_0$ before gradually decreasing, eventually falling below the second-stage temperature in purely hadronic matter in the core. However, the inclusion of hyperons lowers the temperature throughout the stellar matter. This occurs because additional degrees of freedom redistribute the available thermal energy among more particle species, reducing the thermal energy per particle and consequently decreasing the overall temperature at a given density.

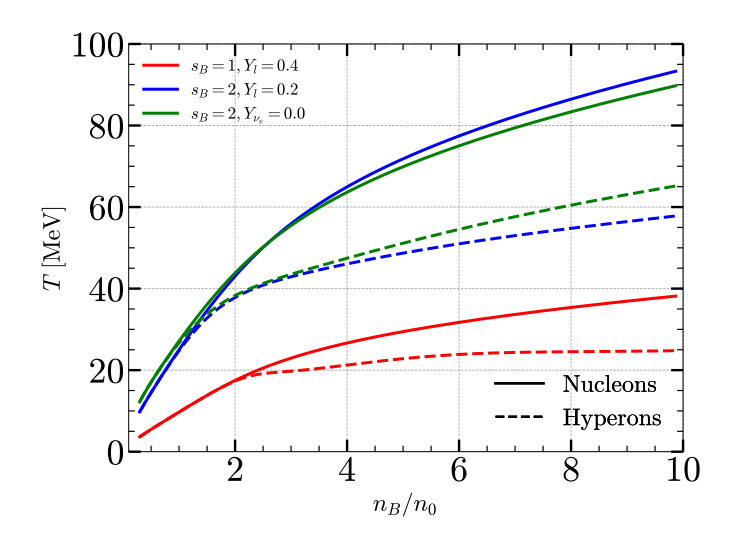


FIG. 2. The temperature distribution in the stellar matter for nucleon-only and nucleon-hyperon admixed PNSs at different stages of the PNS evolution.

Furthermore, the appearance of hyperons increases the specific heat capacity $(C_V \approx (\partial \varepsilon/\partial T)_V)$ of the matter. As a result, more thermal energy is required to raise the temperature. However, since the total thermal energy of the PNSs remains nearly conserved, the temperature decreases to compensate for the increased C_V [7, 8, 16]. Here, the temperature variation follows the pure nucleonic matter phase, except that the temperature is highest for the third stage towards the core.

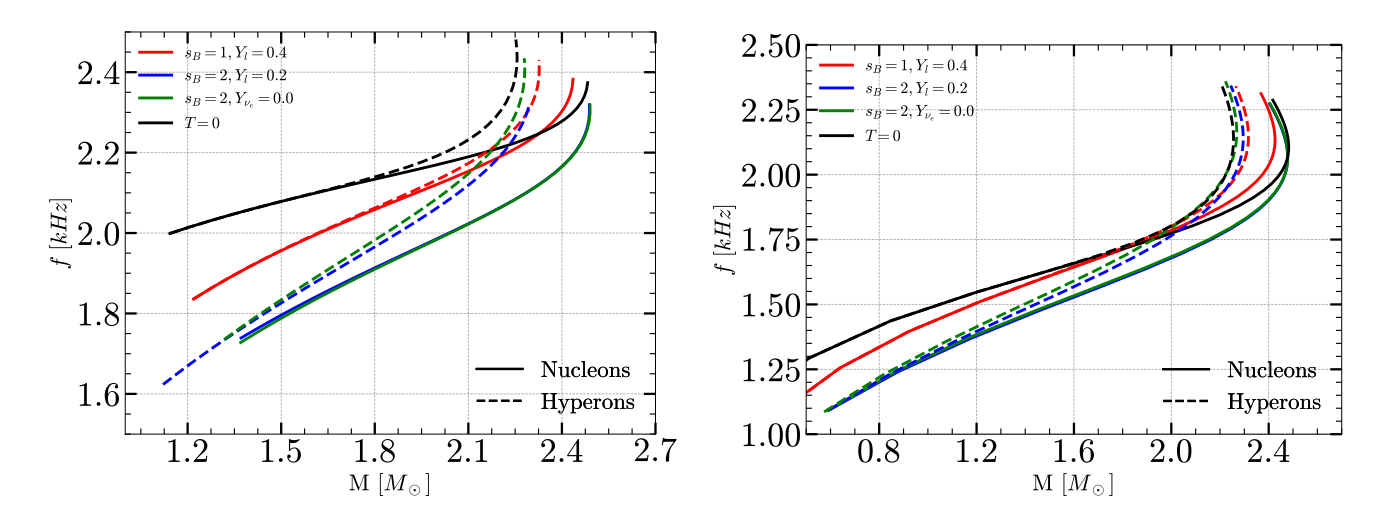


FIG. 3. Gravitational Mass (M) versus fundamental frequency (f) of non-radial oscillation modes for different stages of the PNS evolution with nucleons (solid lines) and with hyperons (dashed lines). The left panel represents results obtained using the Cowling approximation, while the right panel shows calculations based on the full General Relativity (GR) framework.

TABLE III. Stellar maximum mass M_{max} (in M_{\odot}) and the corresponding radius R_{max} (in km) for different configurations studied. Fundamental f-mode frequencies (in kHz) at $1.4 M_{\odot}$ and $2.0 M_{\odot}$ for Nucleons as well as Hyperons using Full GR (GR) and Cowling Approximation (Cow). The damping time is also shown (in sec.).

Model	$M_{max}~(M_{\odot})$	R_{max} (km)	$f_{1.4}$ (GR)	$f_{1.4}$ (Cow)	$f_{2.0}$ (GR)	$f_{2.0}$ (Cow)	P.E. _{1.4} (%)	$P.E{2.0}(\%)$	$\tau_{1.4}~(\mathrm{sec})$
				Nucleons(Hyperon)					
$s_B = 1; Y_l = 0.4$							21.66 (21.66)		
$s_B = 2; Y_l = 0.2$							20.69 (19.59)		
$s_B = 2; \ Y_{\nu_e} = 0$ T = 0		12.03 (11.96)					19.18 (18.67) 28.13 (28.13)		

IV.2. f-mode frequency: GR vs Cowling

In the left panel of Figure 3, the f-mode frequency (in kHz) is shown as a function of the gravitational mass M(in M_{\odot}) for various thermodynamic conditions, including different combinations of s_B and lepton fractions (Y_l and Y_{ν_e}) at β -equilibrium, using the Cowling approximation. This approach neglects metric perturbations, thereby simplifying the oscillation equations. The solid lines correspond to stars composed purely of nucleons, while the dashed lines represent stars with hyperonic degrees of freedom. The right panel presents the corresponding results from full GR calculations, where both fluid and spacetime perturbations are included. Each color represents a distinct thermodynamic scenario: $s_B = 1, Y_l = 0.4$ (red), $s_B = 2, Y_l = 0.2$ (blue), $s_B = 2, Y_{\nu_e} = 0$ (green), and cold matter at T=0 (black). Both panels demonstrate that the Cowling approximation systematically overestimates the f-mode frequencies compared to full GR. At a canonical mass of $1.4 M_{\odot}$, this overestimation reaches up to 28% for both nucleonic and hyperonic stars, as shown in Table III.

Interestingly, the percentage error (P.E.) from the Cowling approximation decreases for the intermediate stages when the star is hot and enlarged, and rises again when the star is cold and catalyzed. This trend is consistent with the known behavior of the Cowling approximation in f-mode studies, where the P.E. tends to decrease for

more massive stars [25, 26, 47]. This behavior arises because f-mode oscillations involve fluid perturbations that peak near the stellar surface, while metric perturbations dominate near the core. In massive NSs, strong surface fluid perturbations couple only weakly to central metric perturbations, making the Cowling approximation more accurate. Furthermore, the same trend is evident at $2.0 M_{\odot}$, where the P.E. continues to decrease for configurations such as $s_B = 2$, $Y_l = 0.2$ and $s_B = 2$, $Y_{\nu_e} = 0$, with the effect being more pronounced in hyperonic stars due to the additional softening of the EoS, increased compactness, and its impact on the gravitational field. The P.E. further decreases when evaluated at the maximum mass configurations for each model, reaching an average of approximately 11.53%. The smallest deviation is observed for the $s_B = 2, Y_l = 0.2$ (hyperons) model, with a relative error of 7.83%, indicating that the Cowling approximation performs well in this thermodynamic setup. This result highlights that, particularly during intermediate evolutionary stages of PNSs, the Cowling approximation can be suitably employed.

Considering that the masses of the PNSs in the second and third stages are nearly identical, we infer that the presence of neutrinos in the second stage increases the P.E. in the f-mode frequency when using the Cowling approximation. In the first stage, where a larger number of neutrinos are trapped, the P.E. is also higher than in the intermediate stages, further supporting the role of

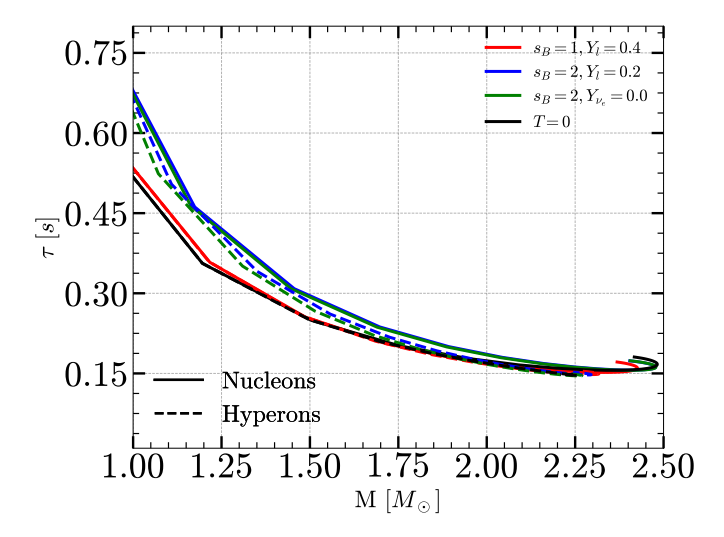


FIG. 4. Damping time (τ) as a function of gravitational mass (M) for non-radial f-mode oscillation at different stages of the PNS evolution for nucleons (solid lines) and hyperons (dashed lines).

neutrinos in increasing the error. This is because neutrinos contribute to the EoS through their pressure, influencing the star's stability, gravitational field, and the restoring force responsible for fluid oscillations. Since the Cowling approximation neglects metric perturbations, it fails to capture the full impact of neutrino-induced effects, leading to less accurate predictions in neutrino-rich environments than full GR calculations [60].

From Figure 3 and Table III, it is clear that at a mass of $1.4\,M_{\odot}$, the f-mode frequencies for nucleonic and hyperonic EoSs are quite close. However, at higher masses such as $2.0 M_{\odot}$, the frequencies become significantly higher for hyperonic EoS, emphasizing the increased influence of EoS softening due to the presence of hyperons. An interesting observation can be made from the GR values in the $f_{1,4}$ column of Table III. The frequencies are lower for configurations with $s_B=2, Y_l=0.2$ and $s_B=2, Y_{\nu_e}=0$ compared to those with $s_B = 2, Y_l = 0.4$ and cold matter at T=0. This effect can be attributed to changes in temperature and compactness during the evolutionary stages of the star due to changes in s_B and Y_l . In the early neutrino-trapping phase (first stage), the high Y_l and trapped neutrinos provide additional pressure support, keeping the EoS relatively stiff.

As the star deleptonizes (second and third stages), neutrinos diffuse out, leading to thermal heating and expansion, which reduces the star's compactness compared to the initial phase. This expansion results in a softened EoS, lowering the sound speed $(c_s^2 = \partial P/\partial \varepsilon)$ and reducing the restoring force for oscillations, thereby decreasing the f-mode frequencies. As deleptonization progresses, the star continues to cool, and once all neutrinos escape, it contracts to form a cold, catalyzed NS. At this stage, the EoS stiffens again due to the increased compactness and the loss of thermal pressure contributions. The stiffer EoS provides stronger pressure support and a higher restor-

ing force, leading to an increase in f-mode frequencies. Thus, the EoS is stiffer in both the first stage (when the temperature is relatively low, see Figure 2) and the final stage (when the star has cooled into a cold, catalyzed NS). This results in higher f-mode frequencies in these phases, whereas the intermediate deleptonization stages—characterized by thermal expansion and a softer EoS—exhibit lower f-mode frequencies, as observed in Ref. [61].

This trend continues even at the maximum mass configuration for nucleonic stars, where the $s_B=1, Y_l=0.4$ and T=0 cases have a frequency of 2.12 and 2.11 kHz, respectively, while the $s_B=2, Y_l=0.2$ and $s_B=2, Y_{\nu_e}=0$ cases show slightly lower frequency of 2.06 kHz. In contrast, for hyperonic stars, the highest frequency at maximum mass is observed for the $s_B=2, Y_{\nu_e}=0$ case at 2.16 kHz, while the lowest is for the cold T=0 case at 2.12 kHz.

Figure 4 shows the damping time τ (in seconds) of f-mode oscillations as a function of gravitational mass M (in M_{\odot}). The legends indicating nucleonic (solid lines) and hyperonic (dashed lines) compositions, as well as the color-coded models based on s_B , Y_l, Y_{ν_e} , and the cold T=0 cases, are the same as those described in the previous figures.

The damping time τ represents the characteristic timescale over which the f-mode oscillation amplitude decays due to gravitational wave emission. As expected, τ decreases monotonically with increasing stellar mass for all compositions and thermodynamic conditions. For a typical NS, the f-mode frequency falls within the range of 1–3 kHz, while the corresponding damping time, τ_f , is typically a few tenths of a second [62, 63]. In our case, the damping time at $1.4 M_{\odot}$ lies in the range of approximately 0.28 to 0.33 seconds and is nearly the same for both nucleonic and hyperonic compositions. At the maximum mass configuration, the damping time decreases to around 0.16 seconds for nucleonic and 0.14 seconds for hyperonic. The trends observed in the f-mode frequencies can be more clearly interpreted by analyzing the role of stellar compactness, as illustrated in Figure 5, which is strongly influenced by the stiffness of the EoS.

Hyperonic EoSs, being softer than nucleonic ones, lead to more compact NSs with smaller radii. This increased compactness influences the dynamics of f-mode oscillations. Since f-mode oscillations involve fluid perturbations peaking near the surface and metric perturbations peaking at the center, the enhanced compactness in hyperonic stars tends to modify the frequency behavior compared to their nucleonic counterparts. For NSs with a nucleonic EoS, which is typically stiffer than its hyperonic admixture counterparts, the larger radius results in a lower mean density. This weakens the restoring force driving fluid oscillations, thereby lowering the f-mode frequencies. The reduced compactness also diminishes metric perturbations and gravitational wave damping, leading to longer damping times. In contrast, hyperonic EoS are generally softer, producing NSs with smaller radii and higher mean densities. This strengthens the

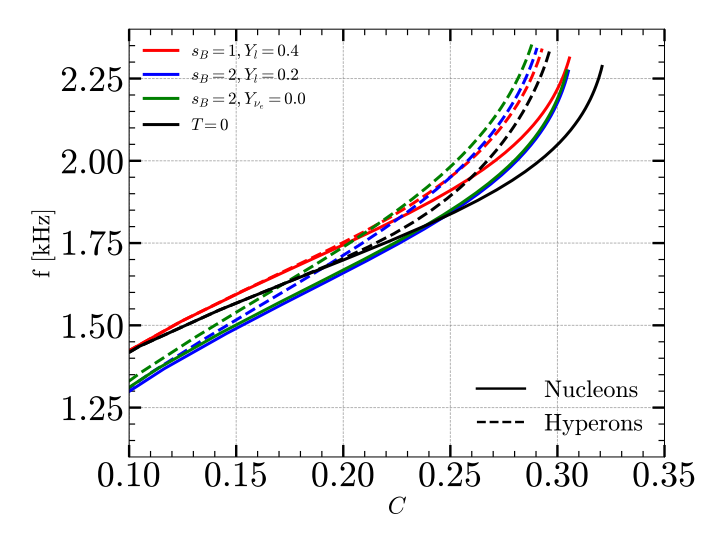


FIG. 5. Non-radial f-mode frequency as a function of Compactness (M/R) at different stages of the PNS evolution for nucleons (solid lines) and hyperons (dashed lines).

restoring force, resulting in higher f-mode frequencies. The increased compactness amplifies metric perturbations, shortening the damping time and enhancing gravitational wave emission [64].

IV.3. Gravitational Wave Asteroseismology

IV.3.1. Universal Relations

In this section, we focus on universal relations, as they are independent of the underlying EoSs. Such relations are particularly valuable because determining NS properties directly from gravitational wave observations is complicated by the significant uncertainty in the EoS of dense matter. Universal relations offer a pathway to bypass this issue by connecting observable quantities in a manner that is largely insensitive to the internal composition of the star. Notable examples include the relation between the f-mode oscillation frequency and the mean stellar density, its dependence on the compactness of the star, and the spacetime (w) mode frequency and damping time as functions of compactness [65–67]

A representative example is shown in the left panel of Figure 6, which illustrates the variation of the fundamental (f) mode oscillation frequency as a function of the square root of the mean density, $\sqrt{M/R^3}$, for NSs under different thermal and compositional conditions. This relation is motivated by the empirical observation that the f-mode frequency scales approximately linearly with the square root of the mean density, as originally proposed by Andersson and Kokkotas [66], which is expressed as:

$$\frac{f}{\text{kHz}} = a + b\sqrt{\frac{M}{R^3}}.$$
(10)

where a and b are 0.22 and 32.16, respectively. The figure includes multiple curves corresponding to different s_B , Y_l ,

and the presence or absence of neutrino trapping. For instance, the red curve corresponds to hot, lepton-rich matter with $s_B=1$ and $Y_l=0.4$, while the blue and green curves show the cases with higher entropy and varying lepton fractions ($s_B=2, Y_l=0.2$ and $Y_{\nu_e}=0$, respectively). The orange line represents the cold NS configuration with T=0. Each thermodynamic configuration includes both nucleonic (solid lines) and hyperonic (dashed lines) EoSs.

Additionally, the figure also includes several model fits for comparison. The dotted black curve labeled "Our fit" corresponds to the empirical relation we derived from our models covering different stages of PNS evolution. which is expressed as:

$$\frac{f}{\text{kHz}} \approx 0.57 + 35.32 \sqrt{\frac{M}{R^3}}.$$
 (11)

While this relation fits well across all the stellar evolutionary stages, it shows a significant deviation from the cold NS data. This indicates that the frequency-compactness relation is not truly universal, but instead depends on the thermodynamic state of the star. The underlying reason for this deviation lies in the internal structure. PNSs are hot, possess high entropy, and contain trapped neutrinos (first and second stages); all of these factors contribute to increased thermal pressure and a stiffer EoS. These factors modify the density and sound speed profiles within the star, generally resulting in lower f-mode frequencies for a given mass and radius.

In contrast, cold NSs are more compact with no thermal or neutrino pressure support, which leads to higher f-mode frequencies. Therefore, a relation derived from PNS models cannot accurately capture the oscillation behavior of cold NSs, emphasizing the need for temperaturedependent relations in gravitational wave asteroseismology. Additionally, the brown and grey dot-dashed curves, labeled "IR1" and "IR2," correspond to predictions from our previous work [47] based on EoSs that include hyperons and Δ baryons. The "IR1" curve represents scenarios without phase transitions, with fit parameters a = 0.44and b = 37.90, while "IR2" (a = 0.39, b = 39.44) reflects cases where the EoS undergoes a phase transition to quark matter. These curves align closely with the behavior of cold NSs, supporting their consistency with the T=0EoS scenarios.

The right panel of Figure 6 presents the normalized damping time of the f-mode, given by the dimensionless quantity $R^4/(M^3\tau)$, plotted as a function of the stellar compactness. This quantity characterizes how efficiently an NS loses energy through gravitational wave emission and is useful for exploring potential universal relations across different star configurations. The colored curves correspond to different thermal stages of PNS evolution, including $s_B = 1, Y_l = 0.4$ (red), $s_B = 2, Y_l = 0.2$ (blue), $s_B = 2, Y_{\nu_e} = 0$ (green), and cold NSs with T = 0 (orange). As before, solid and dashed lines indicate nucleonic and hyperonic EoSs, respectively.

A clear inverse trend is observed: the normalized damping time, $R^4/(M^3\tau)$, decreases with increasing compact-

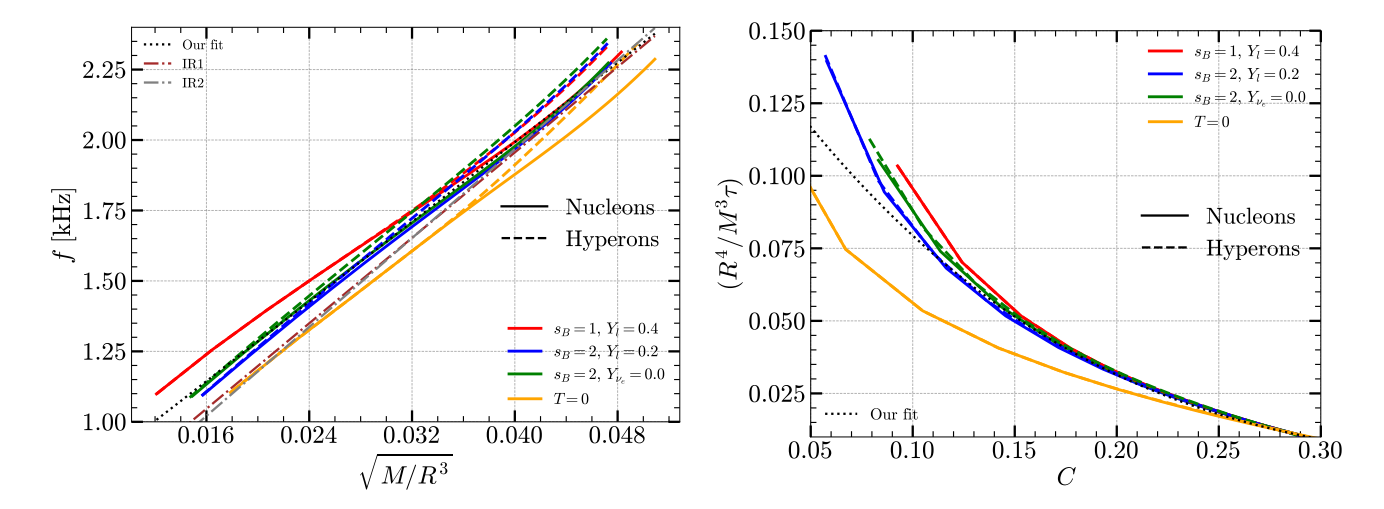


FIG. 6. Left: The f-mode frequency as a function of the mean stellar density. The IR1 (brown) and IR2 (gray) are the fits from the earlier study, represented by a dot-dashed line [47], while "Our fit" (dotted line) represents the fit from the current work. Right: Normalized damping time of the f-mode as a function of the stellar compactness. The solid (dashed) lines correspond to the nucleonic (hyperonic) EoSs for different stages of the PNS evolution.

ness M/R, consistent with the expectation that more compact stars radiate gravitational waves more efficiently. The black dotted curve corresponds to our empirical fit derived from thermal PNS models [68, 69], and is expressed as a cubic polynomial:

$$\frac{R^4}{M^3\tau} = 0.16 - 1.08 \left(\frac{M}{R}\right) + 2.49 \left(\frac{M}{R}\right)^2 - 2.01 \left(\frac{M}{R}\right)^3. \tag{12}$$

This fit captures the overall trend and aligns well with the PNS data, demonstrating a quasi-universal behavior when thermal effects are included.

However, a key finding from the figure is that this fit significantly deviates for cold NSs. The damping times for cold stars fall well below the PNS trend, especially at low compactness. This indicates that the damping timecompactness relation is sensitive to the star's thermal state, and that cold stars cannot be accurately described by a fit calibrated solely on hot stellar configurations. In other words, the apparent universality breaks down once cold NSs are considered. Overall, the figure demonstrates that universal relations constructed for cold NSs are not fully consistent with those for PNSs. The inclusion, cold NS configurations causes a noticeable deviation from the fit obtained using only thermal models, indicating that a single universal relation cannot simultaneously capture the damping behavior of both cold and hot NS phases. This highlights the need for temperature-dependent formulations when modeling gravitational wave damping times.

Figure 7 shows the dimensionless form of the real part of the f-mode frequency, $M\omega_r = 2\pi M f$, plotted against the effective compactness, defined as $\tilde{\eta} = \sqrt{M^3/I}$, where M is the mass and I is the moment of inertia of the NS. This representation is motivated by the search for universal relations that remain largely independent of the underlying EoS. The colored curves correspond to different stages

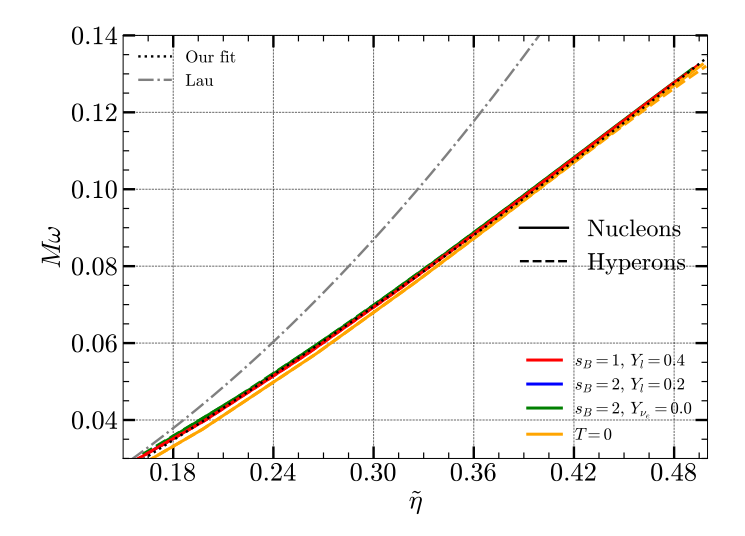


FIG. 7. The dimensionless real part of the f-mode frequency, scaled by mass as $\omega_r = 2\pi f$, is plotted against the effective compactness $\tilde{\eta} = \sqrt{M^3/I}$. The dotted black line represents the fit obtained in this work, while the dot-dashed line corresponds to the fit proposed by Lau et al. [70].

of PNS evolution, including varying entropy and lepton fractions. Solid and dashed lines represent nucleonic and hyperonic EoSs, respectively. The consistency among these curves indicates that the scaled frequency correlates strongly with the effective compactness, regardless of thermal conditions or particle composition.

The black dotted line labeled "Our fit" represents the empirical relation derived in this work, which captures the behavior of $M\omega$ as a function of effective compactness $\tilde{\eta}$. The best-fit linear relation is given by

$$M\omega = -0.011512 + 0.237550\,\tilde{\eta} + 0.108332\,\tilde{\eta}^2 \qquad (13)$$

and it shows excellent agreement with the data across all

the stellar evolutionary stages. In contrast, the dot-dashed grey curve labeled "Lau" represents the universal relation proposed by Lau et al. [70], which shows a noticeable deviation from our fitted relation. Their corresponding fit parameters are a = -0.0047, b = 0.133, and c = 0.0575.

The close clustering of all stellar profiles along our fit line underscores the robustness of this relation across different stellar compositions and evolutionary stages, supporting its applicability in realistic astrophysical scenarios. It also reinforces the idea that the effective compactness $\tilde{\eta}$ is a more suitable scaling variable than the mean density, especially when attempting to construct model-independent EoS relevant for temperature-dependent gravitational wave asteroseismology.

IV.4. p_1 -mode

Next, we focus on calculating the non-radial p_1 -mode (unlike the radial oscillation, here p_1 -modes refers to the pressure modes) for $\ell = 2$. The frequencies and damping times associated with the p_1 -mode provide valuable insights into the internal structure and oscillation behavior of the star. The p_1 -modes are primarily driven by pressure as the dominant restoring force. The p_1 -mode frequency generally lies in the range of 5–7 kHz [26, 47, 71]. However, due to their high frequencies, p_1 -modes are generally not excited during NS mergers [62]. Interestingly, in the context of PNSs, the entropy and the lepton fraction cause a reduction in the p_1 -mode frequencies, making their behavior particularly noteworthy — this aspect will be discussed below. Figure 8 presents the behavior of the p_1 mode in NSs, showing both the oscillation frequency (left panel) and the damping rate $1/\tau$ (right panel) illustrating the variation of the imaginary part of the oscillation frequency, which corresponds to the inverse damping time, $1/\tau$, computed within the full GR framework. Each curve corresponds to different internal conditions of the star, including temperature, composition, and lepton fraction, with a clear visual distinction made through color and linestyle. In both panels, solid lines represent stars composed of nucleonic matter, while dashed lines correspond to configurations that include hyperons. The black lines show results for cold NSs serving as a baseline. In contrast, colored lines correspond to PNS conditions at different s_B and Y_l . Specifically, the red line denotes the first stage $(s_B = 1, Y_l = 0.4)$, the blue line corresponds to the second stage $(s_B = 2, Y_l = 0.2)$, and the green line represents the third stage $(s_B = 2, Y_{\nu_e} = 0.0)$ when all the neutrinos have escaped from the stellar core.

In the left panel, the p_1 -mode frequency increases with stellar mass across all configurations. For cold NSs (shown in black), the frequency reaches significantly higher values, peaking around 6.4 kHz, before slightly decreasing at higher masses. In contrast, hot PNS models exhibit noticeably lower frequencies. Among the configurations studied, those corresponding to the second and third evolutionary stages exhibit the lowest p_1 -mode frequencies. This is primarily due to the expansion of the PNS dur-

ing deleptonization, which reduces its compactness and weakens the restoring pressure forces that drive p-mode oscillations. Additionally, the adiabatic sound speed within the star decreases with increasing s_B , as a higher s_B is associated with enhanced temperatures. This thermal softening of the EoS further contributes to the lowering of oscillation frequencies. These effects are observed both in purely nucleonic matter and in matter that includes hyperonic components. Comprehensive discussions on how stellar composition, thermal effects, and neutrino trapping influence the stellar structure and its oscillatory properties can be found in Refs. [7, 30]. This observed trend is further corroborated by the data presented in Table IV, where the column labeled p_1 (GR) lists the p_1 -mode frequencies calculated for a $1.4\,M_\odot$ configuration. Specifically, the frequencies for the second and third stages for nucleonic matter are 3.77 kHz and 3.63 kHz, respectively, affirming the reduction in frequency during deleptonization.

Another notable observation from Table IV is that the percentage error between the Cowling approximation and full GR is smaller for the first and last stages. Whereas, it increases in the higher s_B cases for the second and the third stages contrary to the f-modes frequencies in Table III, where the Cowling approximation performs better at higher entropy second and third stages. Furthermore, the damping time of the p_1 -mode, τ_{p_1} , for cold NSs is significantly longer than that of the f-mode, consistent with the findings of Refs. [26, 71]. However, this damping time decreases substantially in the intermediate stages of the star's evolution, as shown in Table IV. Similar to the behavior of the p_1 -mode frequency, the presence of hyperons has a minimal impact on the damping time.

TABLE IV. Non-radial p_1 -mode frequency with Cowling approximation (Cow), full (GR) in kHz, percentage error difference P. E., and damping time τ in sec., at $1.4\,M_\odot$ for both nucleonic and hyperonic compositions, computed within the full GR framework. The PE column indicates the percentage by which the Cowling approximation overestimates the p_1 -mode frequency.

Model	p_1 (Cow)	p_1 (GR)	P. E. (%)	τ (sec)			
Nucleons(Hyperons)							
$s_B = 1; Y_l = 0.4$	4.47 (4.48)	4.19 (4.19)	6.64 (6.81)	5.205 (5.173)			
$s_B = 2; Y_l = 0.2$	4.19(4.23)	3.77(3.81)	10.97 (11.02)	4.693 (4.141)			
$s_B = 2; \ Y_{\nu_e} = 0.0$	4.04 (4.10)	3.63(3.69)	11.39 (11.11)	4.511 (3.741)			
T=0	6.32 (6.32)	5.93 (5.93)	6.51 (6.51)	11.856 (11.997)			

IV.5. Radial Profiles

Figure 9 presents the radial displacement eigenfunctions $\xi(r)$ for $1.4 M_{\odot}$ NS models, illustrating how these stars oscillate in their various radial modes. The left plot depicts a purely nucleonic NS, while the second incorporates hyperons alongside nucleons in the stellar composition. Both plots display the dimensionless displacement function against normalized radius (r/R) for

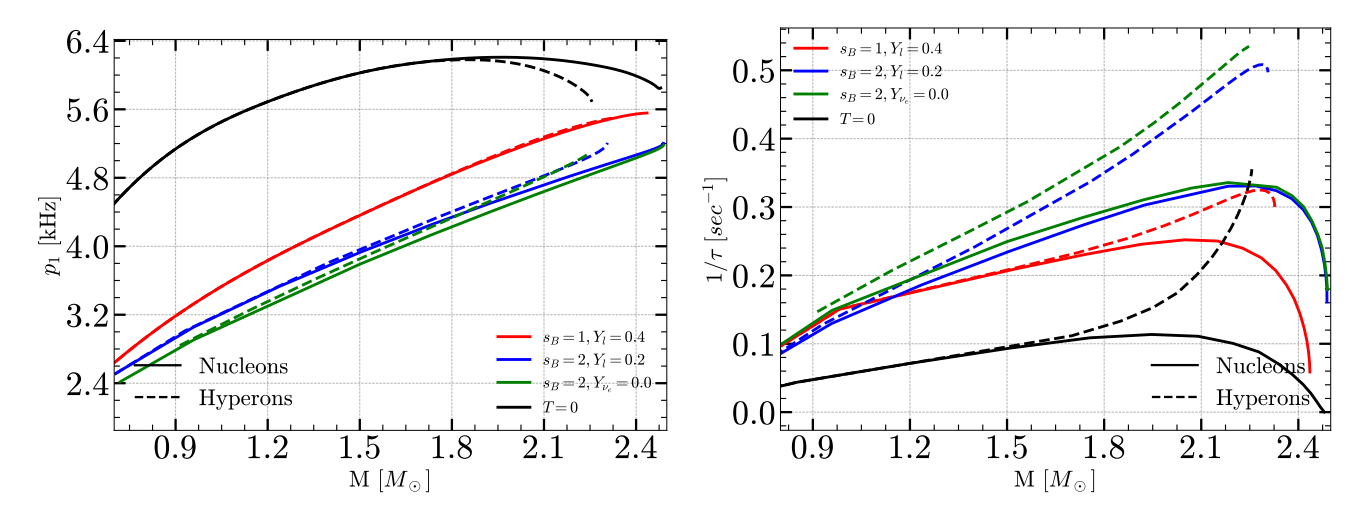


FIG. 8. Left: The p_1 -mode frequency as a function of mass in the full GR framework. Right: Variation of the imaginary part ω of p_1 -mode oscillations (inverse damping time) versus neutron star mass.

different combinations of s_B and Y_l , as well as the cold and catalyzed NS. The fundamental f-mode (n = 0) exhibits a monotonic decrease in displacement from center to surface with no nodes, representing coherent expansion and contraction of the entire star. The inset shows the f-mode displacement close to the surface of the star. The difference between the first stage, with $s_B = 1$ and $Y_l = 0.4$, and the final stage, when the star is cold and catalyzed, is more pronounced compared to the two intermediate stages - $s_B = 2, Y_l = 0.2$ and $s_B = 2, Y_{\nu_e} = 0.0$ - which show almost complete overlap. Since the intermediate stages are characterized by neutrino diffusion, elevated temperatures, and an expanded stellar radius, we can infer that the $\xi(r)$ is sensitive to both the thermal state and the compactness of the star. Apart from the variations in thermal and pressure profiles driven by the change in s_B and Y_l , the speed of sound also evolves throughout the star. This evolution directly influences $\xi(r)$ through modifications in the internal structure and stratification of the stellar matter [20]. Higher-order pmodes (n = 1 - 5) show decreasingly oscillatory behavior with additional nodes, effectively dividing the star into alternating regions of expansion and contraction.

Comparing the nucleonic-only (left plot) and hyperonic models (right plot) reveals subtle but significant differences in their oscillation patterns. The hyperonic model displays slightly higher frequencies for equivalent modes, modified amplitudes, particularly in higher-order modes, and shifted node positions. The inset shows the f-mode displacement, and a clear distinction can be seen in different stages of a PNS evolution along with the cold, catalyzed case, which couldn't be observed in the pure nucleonic case. These variations demonstrate how the presence of hyperons softens the EoS of dense nuclear matter, altering the compressibility and wave propagation characteristics within the star. Such detailed analysis of radial oscillations provides crucial insights into NS structure and composition, with applications to stellar stability assessment, asteroseismology, gravitational wave studies, and PNS evolution following supernova. These oscillation signatures, therefore, serve as valuable probes of matter under extreme conditions.

Figure 10 presents another crucial aspect of NS oscillations through the $\eta(r)$ perturbation function plotted against normalized radius (r/R) for $1.4 M_{\odot}$ NS models. While the previously discussed $\xi(r)$ function represented radial displacement, $\eta(r)$ characterizes the Lagrangian pressure perturbation, offering complementary insights into the stellar pulsation mechanics. The left plot depicts the $\eta(r)$ profiles for a purely nucleonic NS model, while the right plot shows the corresponding profiles for an NS incorporating hyperons alongside nucleons. The amplitude for the final stage, when the star is cold and catalyzed, is higher in the case of nucleons compared to the other stages of the PNS evolution. For intermediate stages of $s_B = 2, Y_l = 0.2$ and $s_B = 2, Y_{\nu_e} = 0.0$, we can see that the fundamental f-mode (n = 0) overlaps, similar to the $\xi(r)$ as seen in Figure 9. The $\eta(r)$ profiles display distinctive features compared to the $\xi(r)$ functions, with more pronounced negative amplitudes near the stellar core and complex oscillatory behavior that intensifies with increasing mode order.

Comparing the nucleonic and hyperonic models reveals subtle but physically significant differences in their $\eta(r)$ patterns, especially for the n=0 case. The inset panels, focusing on the region where 0.48 < r/R < 0.64, highlight variations in the amplitude ranges: approximately -6.4 to -5.6 for the nucleonic as well as the hyperonic model. This slightly broader range in the hyperonic case suggests that the inclusion of exotic particles increases the dynamic response range of pressure perturbations. The introduction of hyperons modifies the pressure distribution throughout the star, altering both the wavelengths and amplitudes of the pressure oscillations. These $\eta(r)$ profiles complement the earlier $\xi(r)$ functions by providing a more complete picture of the thermodynamic response of NS matter to oscillatory perturbations. Together, they enable more robust constraints on the EoS of ultradense

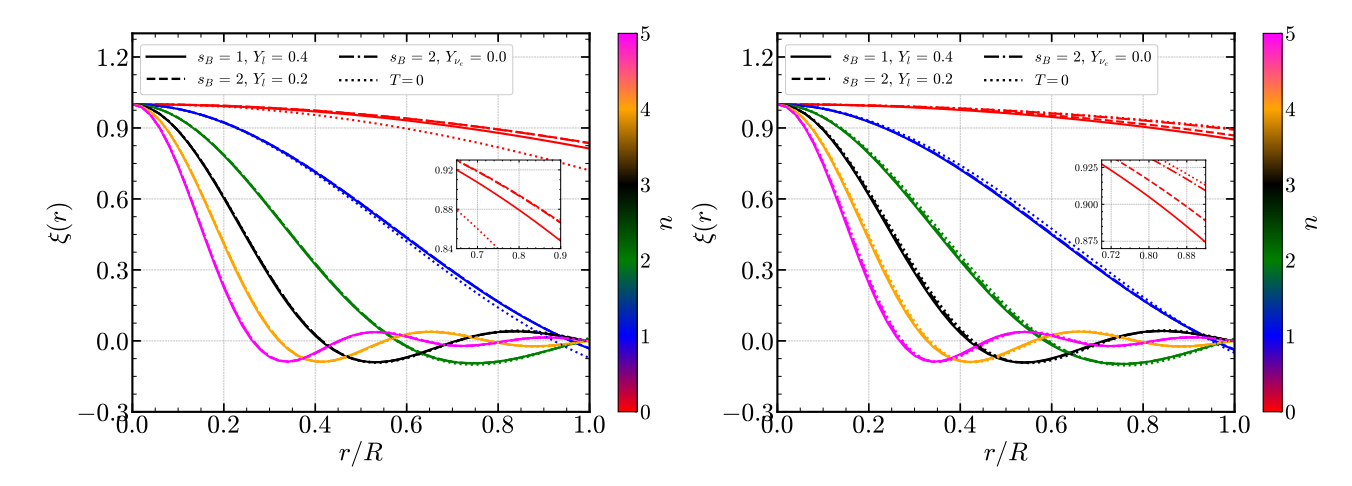


FIG. 9. Left: The radial displacement perturbation $\xi(r) = \Delta r/r$ as a function of dimensionless radius distance r/R for different stages of the PNS evolution. The colorbar represents the modes: f-mode (n=0) and lower-order p-modes (n=1-5) for pure nucleonic EoS. Right: Same as left plot, but for Hyperonic EoSs. All the modes are calculated at $1.4 M_{\odot}$.

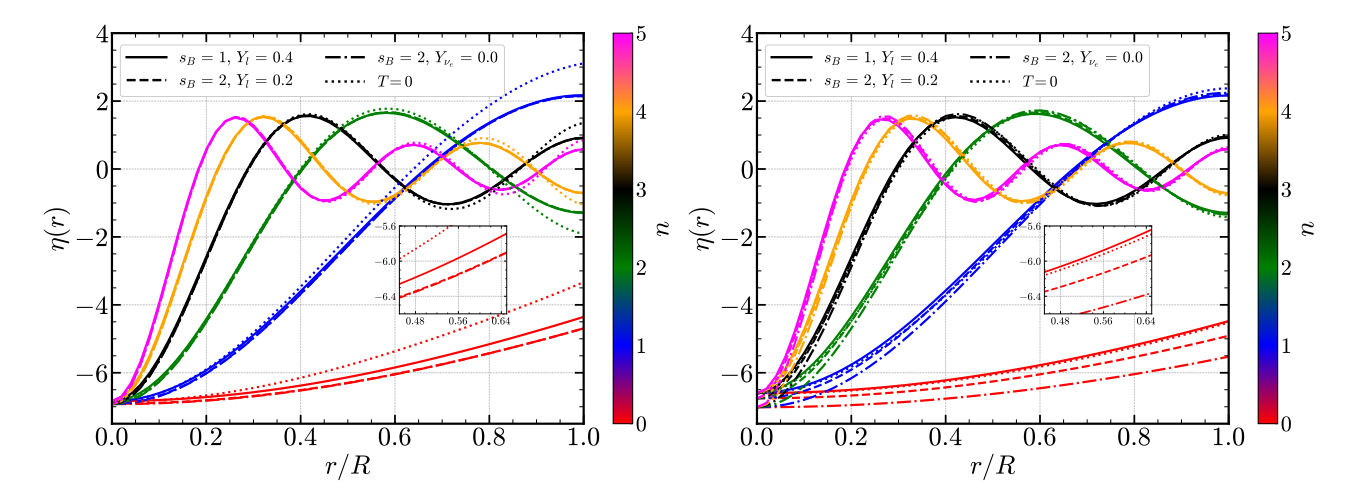


FIG. 10. Left: The radial pressure perturbation $\eta(r) = \Delta r/r$ as a function of dimensionless radius distance r/R for different stages of the PNS evolution. The colorbar represents the modes: f-mode (n=0) and lower-order p-modes (n=1-5) for pure nucleonic EoS. Right: Same as left plot, but for Hyperonic EoSs. All the modes are calculated at $1.4 M_{\odot}$.

matter and reveal how compositional differences manifest in the dynamic properties of NSs, ultimately offering a powerful probe into the physics of matter under conditions unattainable in terrestrial laboratories.

Oscillation amplitudes demonstrate a significant exponential increase toward the stellar surface, driven by the progressively less dense stellar matter. This amplitude enhancement is fundamentally linked to the decreasing density gradient in the outer stellar layers. In PNSs, radial oscillations are particularly pronounced in the less compact outer regions, where the lower-density EoS plays a critical role in determining oscillatory dynamics. The mechanism is particularly notable in trapped-neutrino configurations, where the stellar matter's density stratification creates unique conditions for wave propagation. As the oscillations propagate outward, they experience amplification due to the reduced matter density, which allows for greater displacement and energy transmission. This phenomenon is crucial in understanding the dynamic

behavior of PNSs during their early evolutionary stages, where internal structural changes can significantly impact the stars' overall oscillatory characteristics. The radial mode amplification is not merely a surface effect but a complex interplay between the star's internal density structure, thermal conditions, and the fundamental properties of the stellar EoS. The low-density regions act as preferential zones for oscillatory energy transmission, creating a distinctive pattern of wave propagation that differs markedly from the star's denser core regions.

For comparison of how the profiles change for different stages of PNSs at different fixed masses, we also computed the radial perturbations at $2.0\,M_{\odot}$. The eigenfunctions $\xi(r)$ are more compact and exhibit lower amplitudes compared to the $1.4\,M_{\odot}$ case, reflecting stronger gravitational binding. The effect of hyperons is more pronounced at higher mass, further damping the oscillations, especially in higher-order modes. Node positions shift slightly outward, and differences between thermal stages become less

distinct, indicating that increased compactness dominates over thermal effects in shaping radial oscillations. Compared to the $1.4\,M_\odot$ models, the $2.0\,M_\odot$ NSs show more pronounced oscillatory behavior in $\eta(r)$, likely due to increased compactness and stronger gravitational binding. While the core amplitude range remains nearly unchanged, the overall profiles display enhanced structure and more complex mode features. The cold, catalyzed state continues to exhibit the highest amplitudes, and the overlap of fundamental modes in intermediate stages persists, indicating robust behavior across mass ranges. Hyperonic effects remain significant, though potentially more pronounced at higher central densities.

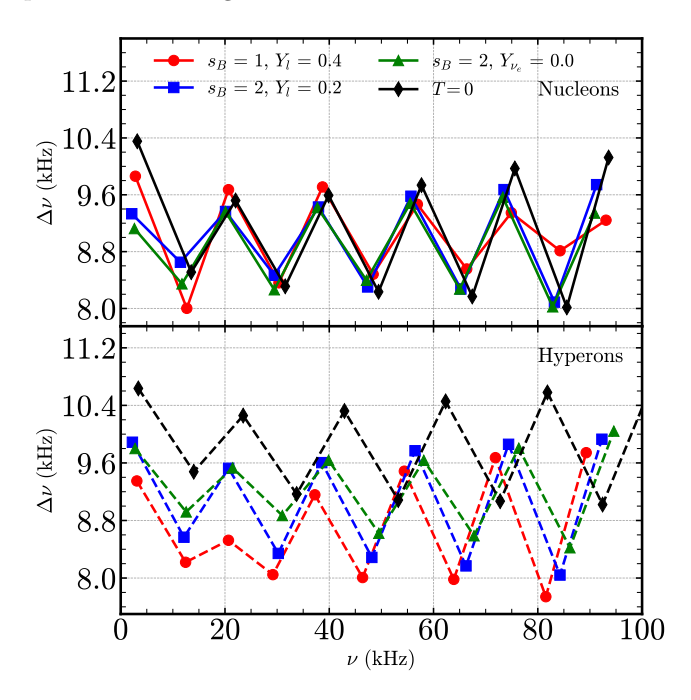


FIG. 11. Frequency difference $\Delta \nu_n = \nu_{n+1}$ - ν_n versus ν_n in kHz for several configurations considered in the text. The upper (lower) panel corresponds to the EoS with nucleons (hyperons) only.

Since the oscillations $\eta(r)$ scale directly with the Lagrangian pressure change ΔP , the amplitudes of successive modes, $\eta_{n+1}(r)$ and $\eta_n(r)$, become more pronounced near the surface. However, because they have opposite signs, their effects cancel each other out, ensuring that the boundary condition P(r=R)=0 holds. As a consequence, the differences $\eta_{n+1}-\eta_n$ and $\xi_{n+1}-\xi_n$ are more responsive to variations in the stellar core. This heightened sensitivity implies that the frequency gap $\Delta \nu_n = \nu_{n+1}-\nu_n$ can act as a key observational marker of the star's innermost layers.

Figure 11 shows the frequency separation, $\Delta \nu_n = \nu_{n+1} - \nu_n$, versus the frequency of different modes ν_n (n=0-9) in kHz for several configurations of PNSs. The upper panel represents the nucleonic configurations, whereas the lower panel corresponds to the hyperonic ones. The first 10 radial modes with f-mode (n=0) and p-modes (n=1-9) calculated at $1.4\,M_\odot$ for nucleonic (hyperonic) configurations are shown in Table V. In the nucleonic

regime, the frequency separation $(\Delta \nu)$ for different stages of a PNS, along with the cold, catalyzed case, displays a relatively smooth, gradual evolution with frequency. However, the hyperon-containing scenario introduces a fundamentally different landscape characterized by pronounced non-linear behaviors and unexpected curvatures. The most unique signatures emerge from the apparent softening of the EoSs, manifested through abrupt changes in the $\Delta\nu$ trend and potential structural instabilities. The cold, catalyzed configuration shows a large, clear, and distinct frequency separation from the different PNS evolutionary stages. These observations suggest that hyperon introduction fundamentally reshapes the stellar internal dynamics, challenging our understanding of dense nuclear matter evolution by inducing significant modifications to sound speed, compressibility, and microscopic stellar structure.

The observed variations in the frequency separation $\Delta \nu$ as ν increases can be mainly attributed to the transition between the crust and the core of the NS, as discussed in Refs. [52–54, 72–74]. In the crust, where the density is relatively low and an inhomogeneous mixture of nuclei and free neutrons prevails, this composite structure significantly influences the oscillation modes. Once the density exceeds a critical threshold, matter becomes uniform in the core, and the resulting crust-core boundary gives rise to mode coupling or conversion effects that lead to fluctuations in the oscillation frequencies. Softer EoSs, which generate steeper density gradients and yield more compact stars, tend to amplify the interaction between crustal and global modes, thereby producing more pronounced fluctuations in $\Delta \nu$. Conversely, stiffer EoSs produce smoother transitions in density and support larger masses and radii, which shifts the oscillation modes and typically results in a reduced frequency separation.

PNSs undergo a series of evolutionary stages that further influence these oscillation characteristics. Each stage—from the high-entropy, neutrino-dominated state to the cooler, neutrino-transparent configuration—introduces changes in the density gradient and compositional profile, thereby affecting the coupling between crustal and core oscillation modes. Consequently, the frequency separation $\Delta\nu$ not only reflects the static properties of the stellar interior but also serves as a dynamic diagnostic tool for probing the evolving structure of the PNS during its early life.

Figure 12 illustrates how the fundamental radial oscillation frequency, ν_0 , of the PNSs varies with stellar mass under different evolutionary conditions. Three distinct stages are represented, corresponding to specific combinations of s_B and Y_l and a phase where $Y_{\nu_e}=0$; when the temperature of the stellar matter reaches its peak and begins to cool down towards the formation of cold, catalyzed, and 'mature' NS configuration. The fundamental frequency, which is sensitive to the star's internal structure and the underlying EoS, varies with mass as well as the star's thermal and compositional profiles.

The dashed lines in the plot represent models that include hyperons, while the solid lines correspond to the

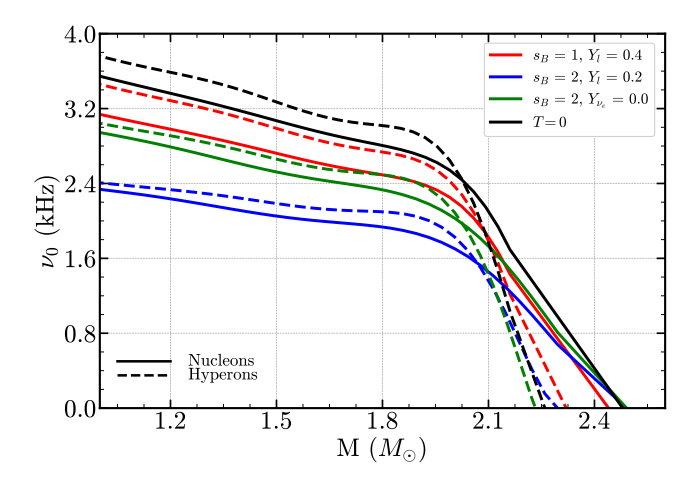


FIG. 12. Radial f-mode (n=0) frequency as a function of mass for different stages of PNS evolution. The solid (dashed) lines correspond to the pure nucleonic (hyperonic) EoSs.

nucleonic-only cases. The softness, due to hyperons, leads to a more compact stellar configuration, resulting in higher fundamental radial oscillation frequencies compared to the nucleonic scenario. In other words, at comparable masses, the hyperonic (dashed) curves exhibit higher frequencies than the nucleonic (solid) ones. This distinct behavior highlights the significant impact of hyperons on the microphysics of dense matter, with the effects being especially pronounced at higher stellar masses where the hyperonic content becomes increasingly relevant to the star's structure and stability. As demonstrated in earlier investigations [53, 73, 75], the f-mode frequency rapidly approaches zero near the point where the maximum numerical NS mass is reached along the MR curve. This behavior is in agreement with the stability criterion, $\partial M/\partial \varepsilon_c > 0$, with ε_c representing the central energy density, which indicates that the star remains stable as long as its mass increases with central density.

TABLE V. 10 lowest-order radial oscillation frequencies, ν in (kHz) for different compositions with nucleons (hyperons). For each EoS, the frequencies are calculated at $1.4\,M_{\odot}$.

2;
0.0
(2.75)
(12.55)
(21.47)
(31.00)
(39.87)
(49.50)
(58.13)
(67.77)
(76.35)
(86.16)

IV.6. Prospects of GW detection

We extend our investigation to evaluate the gravitational wave (GW) energy emission in both the fundamental (f) and first pressure (p_1) modes for 1.4 M_{\odot} for the different stages of the star's evolution. The GW energy is determined from the expression:

$$\frac{E_{\rm GW}}{M_{\odot}c^2} = 3.471 \times 10^{36} \left(\frac{S}{N}\right)^2 \left(\frac{1+4Q^2}{Q^2}\right) \left(\frac{D}{10\,{\rm kpc}}\right)^2 \times \left(\frac{f}{1\,{\rm kHz}}\right)^2 \left(\frac{S_n}{1\,{\rm Hz}^{-1}}\right)^{,}$$
(14)

where S/N signal-to-noise ratio, E_{GW} is the total energy emitted in gravitational waves, $M_{\odot}c^2$ is the solar mass energy equivalent, Q is the quality factor of the oscillation mode related to the dampping time, D is the distance to the source in kiloparsecs (kpc), f is the mode frequency, and S_n is the spectral noise density. Using the formalism in Eq. (14), we estimate the minimum energy required to achieve S/N greater than 5 for various configurations of s_B and Y_l . Frequencies and damping times for each mode are extracted and used to compute the required GW energy for two representative spectral noise densities: $S_n = 2 \times 10^{-23} \; \mathrm{Hz}^{-1}$, corresponding to the current sensitivity of Advanced LIGO/Virgo [76], and $S_n = 1 \times 10^{-24} \; \mathrm{Hz}^{-1}$, representing the capabilities of third-generation detectors like the Einstein Telescope [77], which are shown in Table VI.

For the f-mode, the oscillation frequencies range from 1.45 to 1.60 kHz, with damping times spanning 0.28 to 0.33 seconds across the different thermal configurations. At a distance of 10 kpc, the estimated GW energy required for detection ranges from 7.2×10^{-8} to $8.8 \times 10^{-8} M_{\odot} c^2$ for $S_n = 2 \times 10^{-23}$, and drops significantly to values between 1.82×10^{-10} and 2.22×10^{-10} $M_{\odot}c^2$ for $S_n = 1 \times 10^{-24}$. These energy levels are well within the range of expected GW emission from core-collapse supernova, indicating that f-mode signals from PNSs in our Galaxy are detectable with current and future detectors. For instance, in [78], the authors found that the GW energy emitted during core collapse ranges from approximately 10^{-9} to $10^{-8} M_{\odot} c^2$, based on axisymmetric simulations and depending on the stiffness of the EoS. Similarly, in [79], the predicted GW energy falls within the range 10^{-10} to $10^{-8} M_{\odot} c^2$, depending on the mass of the progenitor star. Other studies reporting estimates within this range include [80, 81] and references therein. At 100 kpc, the required energy increases by four orders of magnitude, reaching approximately 7.2×10^{-6} to $8.8 \times 10^{-6} M_{\odot} c^2$ for current detectors, and 1.82×10^{-8} to $2.22 \times 10^{-8} M_{\odot} c^2$ for third-generation detectors. Although this represents a more challenging detection scenario, the lower thresholds associated with advanced detectors may still permit observability under favorable conditions. At 15 Mpc, the energy thresholds become significantly more demanding: values of 1.64×10^{-1} to $1.99 \times 10^{-1} M_{\odot} c^2$ are required for Advanced LIGO, which are prohibitively high. How-

TABLE VI. Gravitational wave energy estimates for various evolutionary stages of a PNS with a mass of $1.4\,M_{\odot}$ are presented at different source distances. The associated oscillation frequencies (in kHz) and damping times (in sec) are also provided for a range of spectral noise densities.

Distance	Model	S_1	$S_n = 2 \times 10^{-23} \text{ Hz}^{-1}$			$S_n = 1 \times 10^{-24} \text{ Hz}^{-1}$			
Distance	Model	f (kHz)	τ (s)	$E_{\rm GW}/(M_{\odot}c^2)$	f (kHz)	τ (s)	$E_{\rm GW}/(M_{\odot}c^2)$		
f-mode with Nucleons									
10 kpc	$(s_B = 1; Y_l = 0.4)$	1.57	0.28	8.5×10^{-8}	1.57	0.28	2.13×10^{-10}		
	$(s_B=2;\ Y_l=0.2)$	1.45	0.33	7.2×10^{-8}	1.45	0.33	1.82×10^{-10}		
	$(s_B = 2; Y_{\nu_e} = 0.0)$	1.46	0.33	7.3×10^{-8}	1.46	0.33	1.84×10^{-10}		
	(T=0)	1.60	0.28	8.8×10^{-8}	1.60	0.28	2.22×10^{-10}		
	$(s_B = 1; Y_l = 0.4)$	1.57	0.28	8.5×10^{-6}	1.57	0.28	2.13×10^{-8}		
100 kpc	$(s_B=2; Y_l=0.2)$	1.45	0.33	7.2×10^{-6}	1.45	0.33	1.82×10^{-8}		
100 kpc	$(s_B = 2; Y_{\nu_e} = 0.0)$	1.46	0.33	7.3×10^{-6}	1.46	0.33	1.84×10^{-8}		
	(T=0)	1.60	0.28	8.8×10^{-6}	1.60	0.28	2.22×10^{-8}		
	$(s_B = 1; Y_l = 0.4)$	1.57	0.28	1.92×10^{-1}	1.57	0.28	4.81×10^{-4}		
15 Mpc	$(s_B=2;\ Y_l=0.2)$	1.45	0.33	1.64×10^{-1}	1.45	0.33	4.10×10^{-4}		
тэ мрс	$(s_B = 2; Y_{\nu_e} = 0.0)$	1.46	0.33	1.66×10^{-1}	1.46	0.33	4.16×10^{-4}		
	(T=0)	1.60	0.28	1.99×10^{-1}	1.60	0.28	4.99×10^{-4}		
		p_1 -1	mode with	Nucleons					
	$(s_B = 1; Y_l = 0.4)$	4.19	5.20	6.0×10^{-7}	4.19	5.20	1.52×10^{-9}		
$10 \; \mathrm{kpc}$	$(s_B=2;\ Y_l=0.2)$	3.77	4.69	5.0×10^{-7}	3.77	4.69	1.23×10^{-9}		
то крс	$(s_B = 2; Y_{\nu_e} = 0.0)$	3.62	4.51	4.5×10^{-7}	3.62	4.51	1.13×10^{-9}		
	(T=0)	5.93	11.85	1.2×10^{-6}	5.93	11.85	3.05×10^{-9}		
	$(s_B = 1; Y_l = 0.4)$	4.19	5.20	6.0×10^{-5}	4.19	5.20	1.52×10^{-7}		
100 kpc	$(s_B=2; Y_l=0.2)$	3.77	4.69	5.0×10^{-5}	3.77	4.69	1.23×10^{-7}		
	$(s_B = 2; Y_{\nu_e} = 0.0)$	3.62	4.51	4.5×10^{-5}	3.62	4.51	1.13×10^{-7}		
	(T=0)	5.93	11.85	1.2×10^{-4}	5.93	11.85	3.05×10^{-7}		
	$(s_B = 1; Y_l = 0.4)$	4.19	5.20	1.37	4.19	5.20	3.42×10^{-3}		
15 Mpc	$(s_B = 2; Y_l = 0.2)$	3.77	4.69	1.11	3.77	4.69	2.77×10^{-3}		
15 Mpc	$(s_B = 2; Y_{\nu_e} = 0.0)$	3.62	4.51	1.02	3.62	4.51	2.55×10^{-3}		
	(T=0)	5.93	11.85	2.74	5.93	11.85	6.80×10^{-3}		

ever, with the improved sensitivity of the Einstein Telescope, the required energy drops to between 4.10×10^{-4} and $4.99 \times 10^{-4} \, M_{\odot} c^2$. While still high, such values are marginally within reach for extremely energetic or repeated events, suggesting that the f-mode from extragalactic sources may be detected by future observatories under exceptional circumstances.

The p_1 mode presents higher frequencies, ranging from 3.62 to 5.93 kHz, and significantly longer damping times between 4.51 and 11.85 seconds. As a result, the energy required for detection is generally higher. At 10 kpc, the required energy ranges from 4.5×10^{-7} to $1.2 \times 10^{-6} \, M_{\odot} c^2$ for $S_n = 2 \times 10^{-23}$ and from 1.13×10^{-9} to $3.05 \times 10^{-9} \, M_{\odot} c^2$ for $S_n = 1 \times 10^{-24}$. These values are close to the expected energy output from PNS oscillations following a supernova, making the detection of p_1 -modes feasible, especially with third-generation detectors [78, 80, 82]. At 100 kpc, the required GW energy increases to between 4.5×10^{-5} and $1.2 \times 10^{-4} M_{\odot} c^2$ for Advanced LIGO, and 1.13×10^{-7} to $3.05 \times 10^{-7} M_{\odot}c^2$ for the Einstein Telescope. While detection becomes challenging at this distance with current instruments, advanced detectors may still succeed in capturing such signals from moderately distant sources. The scenario at 15 Mpc remains extremely demanding. Advanced LIGO's required energy ranges from 1.02 to 2.74 $M_{\odot}c^2$, far exceeding realistic emission levels. For the Einstein Telescope, the energy requirement is reduced to 2.55×10^{-3} to $6.80\times 10^{-3}~M_{\odot}c^2$, which, though still large, brings the possibility of detection marginally closer, particularly in the case of strong excitation mechanisms or multiple sources contributing to the signal.

In summary, the f and p_1 mode oscillations of PNSs determined are within the detection limits of current GW observatories for Galactic sources, and future detectors like the Einstein Telescope are expected to considerably extend this reach, potentially up to the outskirts of the Local Group. However, for extragalactic distances such as 15 Mpc, only extremely energetic events or stacked signals from multiple PNSs might yield detectable gravitational wave signatures. These results reinforce the importance of continuous monitoring by highly sensitive instruments and highlight the diagnostic potential of GW observations in probing the thermal and compositional evolution of NSs shortly after their birth.

V. SUMMARY AND OUTLOOK

The present work represents a natural extension of Ref. [24], which investigated non-radial oscillations during similar stages of PNS evolution using fully GR calculations. However, the study did not incorporate neutrino effects and was limited to nucleonic matter, neglecting the presence of hyperons. Building upon this foundation, this study investigates the radial and non-radial oscillations during the evolution of a PNS, from its birth as a neutrino-rich object to its transition into a neutrino-transparent, cold, catalyzed NS. Our results show that the presence of trapped neutrinos at low s_B increases the stellar compactness, as seen in the early post-bounce phase. As deleptonization proceeds and s_B rises, the internal temperature increases, leading to an expanded stellar radius and reduced compactness, characteristic of the intermediate evolutionary stages. Once the neutrinos have fully escaped from the core, the star begins to contract, ultimately forming a cold NS at T=0.

The structural evolution of PNSs into cold, catalyzed NSs, compared with observational mass, radius confidence contours, reveals that, beyond thermal effects, the inclusion of hyperons leads to a reduction in both stellar mass and radius, as expected [83]. Additionally, hyperons decrease the temperature distribution within the stellar matter by lowering the thermal energy per baryon due to their impact on the entire composition and thermodynamics of the EoS [7].

By analyzing non-radial oscillations through the f- and p_1 -modes (where p_1 -mode refers to pressure mode) using both the Cowling approximation and the full GR approach, we observed that the Percentage Error (P.E.) in the f-mode frequencies is minimal during the deleptonization phase, when the star is hot and expanded, thus favoring the Cowling approximation. This suggests that gravitational perturbations are relatively insignificant during neutrino diffusion when the stellar matter is heated. As the star cools and reaches a catalyzed configuration, gravitational effects become more pronounced, leading to a higher P.E., since the Cowling approximation neglects these perturbations. In Ref. [50, 84], the authors provide an extensive comparison between the full GR framework and the Cowling approximation across various oscillation modes, offering valuable insights into the behavior and magnitude of the P.E. Additional studies on stellar oscillations, including both theoretical foundations and mode classifications, can be found in Ref. [66] and references therein. The results obtained in these references qualitatively agree with our findings.

In contrast, the analysis of the p_1 -mode frequencies reveals a different trend. The P.E. is highest during the intermediate stages of the star's evolution, while the lowest P.E. occurs when the star reaches the cold, catalyzed configuration. This discrepancy arises because p_1 -modes are more sensitive to pressure gradients within the star. During the intermediate stages, the balance of temperature, pressure, and density becomes more complex as the star undergoes deleptonization, making it harder for both the Cowling and full GR approaches to accurately capture the density and pressure variations [85]. As the star stabilizes and cools, the pressure and density gradients become more straightforward, allowing both approaches to more accurately describe the oscillations, resulting in

a reduction in the P.E.. In Ref. [30], the authors demonstrate that thermal pressure and the stellar composition significantly alter the non-radial frequencies during deleptonization, in agreement with our findings. Comparison between f- and p_1 -modes for PNSs can also be found in [50].

While the inclusion of hyperons modifies the EoS by softening it, leading to more compact stellar configurations, our analysis shows that the resulting changes in the f- and p_1 -mode frequencies are relatively modest. This indicates that, within the mass range and thermal conditions considered in studying the stellar evolution, these modes are not strongly sensitive to variations in core compositions. The similarities observed between nucleonic and hyperonic models suggest that, although hyperons influence the overall structure, their effect on the non-radial oscillation spectrum remains limited. We note, however, that larger deviations may arise in more massive stars or in modes such as q-modes, which are more sensitive to composition gradients and thermal stratification—an investigation that lies beyond the scope of the present study.

We tested our EoSs against several universal relations to assess the influence of entropy and lepton fraction. From the behavior of the f-mode frequencies and damping times, we found that no existing universal relation accurately describes both PNSs through to their transition into cold, catalyzed NSs simultaneously. This underscores the need to incorporate temperature and neutrino effects when modeling gravitational-wave damping time. Motivated by this, we derived a new, more robust universal relation—presented in Equation (13) and illustrated in Figure 7—by fitting to PNS data. This result accounts for the thermal effects and the neutron presence associated with PNSs and their evolution. Although this relation remains model-dependent until tested against a wider range of PNS models, it offers a more realistic description than those derived solely from cold NS configurations.

By analyzing the radial displacement $\xi(r)$ and pressure perturbation $\eta(r)$ eigenfunctions of radial profiles, we identified distinct signatures in the oscillation patterns associated with the thermal and compositional evolution of the star. Our results show that the inclusion of hyperons leads to a more compact configuration and hence higher oscillation frequencies. The evolution of the fundamental f-mode and its separation from higher p-modes reveal key structural changes, particularly near the crust-core interface, and provide a sensitive probe of the internal stellar dynamics.

The frequency separation $\Delta\nu$ exhibits non-linear behavior, especially in hyperonic models, offering insights into the softness/stiffness of the EoS and the crust–core coupling during PNS evolution. Furthermore, the correlation of the fundamental mode frequency ν_0 with stellar mass highlights the stabilizing or destabilizing effects of thermal and compositional changes, with the f-mode frequency vanishing near the maximum mass limit, consistent with the stability criterion.

Finally, we estimate the GW energy required for detec-

tion within our model by combining the f- and p_1 -mode non-radial frequencies of each stellar configuration with the spectral noise densities of Advanced LIGO/Virgo [76] and the next-generation Einstein Telescope [77], to evaluate the sensitivity of these detectors. The results indicate that the f- and p_1 -mode oscillations of PNSs lie within the detection range of current GW observatories for galactic events, while next-generation detectors like the Einstein Telescope are expected to significantly extend this reach to extragalactic distances.

As a future direction, extending this analysis to include more exotic phases of matter such as color-superconducting (CSC) quark phases [86, 87], as well as the potential influence of dark matter [18] on PNS oscillation spectra would provide valuable insights into the internal dynamics and composition of NS. Exploring both radial and non-radial modes in hybrid stars and twin-star configurations will further enhance our understanding of the dense matter EoS and its astrophysical manifestations. These investigations may open new observational windows through gravitational wave asteroseismology and contribute to constraining the fundamental physics governing compact stars.

ACKNOWLEDGEMENT

A.I. acknowledges financial support from the São Paulo State Research Foundation (FAPESP), Grant No. 2023/09545-1. I.A.R. acknowledges support from the Alexander von Humboldt Foundation. T. F. also thanks the financial support from Improvement of Higher Education Personnel CAPES (Finance Code 001), the National Council for Scientific and Technological Development (CNPq) under Grants Nos. 306834/2022-7, and FAPESP (Grant 2019/07767-1). Y. Lim is supported by the National Research Foundation of Korea(NRF) grant funded by the Korea government (MSIT) (No. RS-2024-00457037) and by Global - Learning & Academic research institution for Master's PhD students, and Postdocs(LAMP) Program of the National Research Foundation of Korea(NRF) grant funded by the Ministry of Education(No. RS-2024-00442483). Y. Lim is also supported by the Yonsei University Research Fund of 2024-22-0121.

- [1] H.-T. Janka, Ann. Rev. Nucl. Part. Sci. 62, 407–451 (2012), arXiv:1206.2503 [astro-ph.SR].
- [2] K. Kotake, K. Sato, and K. Takahashi, Rept. Prog. Phys. 69, 971–1144 (2006), arXiv:astro-ph/0509456.
- [3] G. G. Raffelt, Phys. Rept. 198, 1–113 (1990).
- [4] G. Raffelt and D. Seckel, Phys. Rev. Lett. 60, 1793 (1988).
- [5] K. Hirata et al. (Kamiokande-II), Phys. Rev. Lett. 58, 1490–1493 (1987).
- [6] K. S. Hirata et al., Phys. Rev. D 38, 448–458 (1988).
- [7] J. A. Pons, S. Reddy, M. Prakash, J. M. Lattimer, and J. A. Miralles, Astrophys. J. 513, 780 (1999), arXiv:astroph/9807040.
- [8] M. Prakash, I. Bombaci, M. Prakash, P. J. Ellis, J. M. Lattimer, and R. Knorren, Phys. Rept. 280, 1–77 (1997), arXiv:nucl-th/9603042.
- [9] D. Vartanyan, A. Burrows, D. Radice, A. M. Skinner, and J. Dolence, Mon. Not. Roy. Astron. Soc. 482, 351–369 (2019), arXiv:1809.05106 [astro-ph.HE].
- [10] G. Camelio, A. Lovato, L. Gualtieri, O. Benhar, J. A. Pons, and V. Ferrari, Phys. Rev. D 96, 043015 (2017), arXiv:1704.01923 [astro-ph.HE].
- [11] K. Nakazato and H. Suzuki, Astrophys. J. 878, 25 (2019), arXiv:1905.00014 [astro-ph.HE].
- [12] J. M. Lattimer and M. Prakash, Phys. Rep. 621, 127 (2016).
- [13] M. Oertel, M. Hempel, T. Klähn, and S. Typel, Rev. Mod. Phys. 89, 015007 (2017).
- [14] A. Issifu, K. D. Marquez, M. R. Pelicer, and D. P. Menezes, Mon. Not. Roy. Astron. Soc. 522, 3263–3270 (2023), arXiv:2302.04364 [nucl-th].
- [15] A. Issifu, D. P. Menezes, Z. Rezaei, and T. Frederico, JCAP 01, 024 (2025), arXiv:2405.10386 [nucl-th].
- [16] A. R. Raduta, M. Oertel, and A. Sedrakian, Mon. Not. Roy. Astron. Soc. 499, 914–931 (2020), arXiv:2008.00213 [nucl-th].

- [17] S. Kunkel, S. Wystub, and J. Schaffner-Bielich, Phys. Rev. C 111, 035807 (2025), arXiv:2411.14930 [nucl-th].
- [18] A. Issifu, P. Thakur, F. M. da Silva, K. D. Marquez, D. P. Menezes, M. Dutra, O. Lourenço, and T. Frederico, Phys. Rev. D 111, 083026 (2025), arXiv:2412.17946 [hep-ph].
- [19] T. T. Sun, Z. Y. Zheng, H. Chen, J. B. Wei, G. F. Burgio, and H. J. Schulze, Phys. Rev. D 111, 043008 (2025), arXiv:2408.06599 [nucl-th].
- [20] D. Gondek, P. Haensel, and J. L. Zdunik, Astron. Astrophys. 325, 217–227 (1997), arXiv:astro-ph/9705157.
- [21] K. D. Kokkotas and J. Ruoff, Astron. Astrophys. 366, 565 (2001), arXiv:gr-qc/0011093.
- [22] H. Sotani and K. Sumiyoshi, Mon. Not. Roy. Astron. Soc. 507, 2766–2776 (2021), arXiv:2108.02484 [astro-ph.HE].
- [23] M. C. Rodriguez, I. F. Ranea-Sandoval, C. Chirenti, and D. Radice, Mon. Not. Roy. Astron. Soc. 523, 2236–2246 (2023), arXiv:2304.00033 [astro-ph.HE].
- [24] N. Barman, B. K. Pradhan, and D. Chatterjee, (2024), arXiv:2408.00739 [astro-ph.HE].
- [25] B. K. Pradhan, D. Chatterjee, M. Lanoye, and P. Jaikumar, Phys. Rev. C 106, 015805 (2022), arXiv:2203.03141 [astro-ph.HE].
- [26] A. Kunjipurayil, T. Zhao, B. Kumar, B. K. Agrawal, and M. Prakash, Phys. Rev. D 106, 063005 (2022), arXiv:2205.02081 [nucl-th].
- [27] D. G. Roy, T. Malik, S. Bhattacharya, and S. Banik, Astrophys. J. 968, 124 (2024), arXiv:2312.02061 [astro-ph.HE].
- [28] Z.-Y. Zheng, T.-t. Sun, H. Chen, J.-B. Wei, X.-P. Zheng, H. J. Schulze, and G. F. Burgio, (2025), arXiv:2505.10133 [astro-ph.HE].
- [29] D. Kumar, A. Karan, A. Verma, H. Mishra, and R. Mallick, Phys. Rev. C 111, 055805 (2025), arXiv:2409.01785 [astro-ph.HE].
- [30] V. Ferrari, G. Miniutti, and J. A. Pons, Mon. Not. Roy. Astron. Soc. 342, 629 (2003), arXiv:astro-ph/0210581.

- [31] B. D. Serot and J. D. Walecka, Int. J. Mod. Phys. E 6, 515–631 (1997), arXiv:nucl-th/9701058.
- [32] D. P. Menezes, Universe 7, 267 (2021), arXiv:2106.09515 [astro-ph.HE].
- [33] I. Bombaci, JPS Conf. Proc. 17, 101002 (2017), arXiv:1601.05339 [nucl-th].
- [34] G. A. Lalazissis, T. Nikšić, D. Vretenar, and P. Ring, Phys. Rev. C 71, 024312 (2005).
- [35] M. Dutra, O. Lourenço, J. S. Sá Martins, A. Delfino, J. R. Stone, and P. D. Stevenson, Phys. Rev. C 85, 035201 (2012).
- [36] J. M. Lattimer and Y. Lim, Astrophys. J. 771, 51 (2013), arXiv:1203.4286 [nucl-th].
- [37] B. T. Reed, F. J. Fattoyev, C. J. Horowitz, and J. Piekarewicz, Phys. Rev. Lett. 126, 172503 (2021).
- [38] N. K. Glendenning and S. A. Moszkowski, Phys. Rev. Lett. 67, 2414–2417 (1991).
- [39] S. Weissenborn, D. Chatterjee, and J. Schaffner-Bielich, Nucl. Phys. A 881, 62–77 (2012), arXiv:1111.6049 [astro-ph.HE].
- [40] L. L. Lopes, K. D. Marquez, and D. P. Menezes, Phys. Rev. D 107, 036011 (2023), arXiv:2211.17153 [hep-ph].
- [41] B. P. Abbott et al. (LIGO Scientific, Virgo), Phys. Rev. Lett. 119, 161101 (2017), arXiv:1710.05832 [gr-qc].
- [42] B. P. Abbott et al. (LIGO Scientific, Virgo), Phys. Rev. Lett. 121, 161101 (2018), arXiv:1805.11581 [gr-qc].
- [43] T. E. Riley et al., Astrophys. J. Lett. 918, L27 (2021), arXiv:2105.06980 [astro-ph.HE].
- [44] M. C. Miller et al., Astrophys. J. Lett. 918, L28 (2021), arXiv:2105.06979 [astro-ph.HE].
- [45] T. E. Riley et al., Astrophys. J. Lett. 887, L21 (2019), arXiv:1912.05702 [astro-ph.HE].
- [46] M. Miller et al., Astrophys. J. Lett. 887, L24 (2019), arXiv:1912.05705 [astro-ph.HE].
- [47] I. A. Rather, K. D. Marquez, P. Thakur, and O. Lourenço, (2024), arXiv:2412.12002 [astro-ph.HE].
- [48] T. Zhao, C. Constantinou, P. Jaikumar, and M. Prakash, Phys. Rev. D 105, 103025 (2022), arXiv:2202.01403 [gr-qc].
- [49] A. Kumar, P. Thakur, and M. Sinha, Mon. Not. Roy. Astron. Soc. 530, 501–513 (2024), arXiv:2404.01252 [astro-ph.HE].
- [50] V. B. Thapa, M. V. Beznogov, A. R. Raduta, and P. Thakur, Phys. Rev. D 107, 103054 (2023), arXiv:2302.11469 [nucl-th].
- [51] J. M. Bardeen, K. S. Thorne, and D. W. Meltzer, Astrophys. J. 145, 505 (1966).
- [52] I. A. Rather, K. D. Marquez, G. Panotopoulos, and I. Lopes, Phys. Rev. D 107, 123022 (2023), arXiv:2303.11006 [nucl-th].
- [53] I. A. Rather, K. D. Marquez, B. C. Backes, G. Panotopoulos, and I. Lopes, JCAP 05, 130 (2024), arXiv:2401.07789 [nucl-th].
- [54] N. K. Glendenning, Compact stars: Nuclear physics, particle physics, and general relativity (1997).
- [55] T. E. Riley et al., Astrophys. J. Lett. 887, L21 (2019), arXiv:1912.05702 [astro-ph.HE].
- [56] T. E. Riley et al., Astrophys. J. Lett. 918, L27 (2021), arXiv:2105.06980 [astro-ph.HE].
- [57] D. Choudhury et al., The Astrophysical Journal Letters 971, L20 (2024).
- [58] J. R. Oppenheimer and G. M. Volkoff, Phys. Rev. 55, 374–381 (1939).
- [59] J. R. Oppenheimer and G. M. Volkoff, Phys. Rev. 55, 374–381 (1939).

- [60] H. Sotani and T. Takiwaki, Phys. Rev. D 102, 063025 (2020), arXiv:2009.05206 [astro-ph.HE].
- [61] T. Zhao and J. M. Lattimer, Phys. Rev. D 106, 123002 (2022), arXiv:2204.03037 [astro-ph.HE].
- [62] K. D. Kokkotas and B. G. Schmidt, Living Rev. Rel. 2, 2 (1999), arXiv:gr-qc/9909058.
- [63] B. K. Pradhan and D. Chatterjee, Phys. Rev. C 103, 035810 (2021), arXiv:2011.02204 [astro-ph.HE].
- [64] L. Lindblom and S. L. Detweiler, Astrophys. J. Suppl. 53, 73–92 (1983).
- [65] O. Benhar, E. Berti, and V. Ferrari, Mon. Not. Roy. Astron. Soc. 310, 797–803 (1999), arXiv:gr-qc/9901037.
- [66] N. Andersson and K. D. Kokkotas, Mon. Not. Roy. Astron. Soc. 299, 1059–1068 (1998), arXiv:gr-qc/9711088.
- [67] C. Chirenti, G. H. de Souza, and W. Kastaun, Phys. Rev. D 91, 044034 (2015), arXiv:1501.02970 [gr-qc].
- [68] G. Lioutas and N. Stergioulas, Gen. Rel. Grav. 50, 12 (2018), arXiv:1709.10067 [gr-qc].
- [69] H. Sotani, Phys. Rev. D 103, 123015 (2021).
- [70] H. K. Lau, P. T. Leung, and L. M. Lin, The Astrophysical Journal 714, 1234 (2010).
- [71] P. Thakur, S. Chatterjee, K. K. Nath, and R. Mallick, Phys. Rev. D 110, 103045 (2024), arXiv:2407.12601 [gr-qc].
- [72] S. Sen, S. Kumar, A. Kunjipurayil, P. Routaray, S. Ghosh, P. J. Kalita, T. Zhao, and B. Kumar, Galaxies 11, 60 (2023), arXiv:2205.02076 [nucl-th].
- [73] P. Routaray, H. C. Das, S. Sen, B. Kumar, G. Panotopoulos, and T. Zhao, Phys. Rev. D 107, 103039 (2023), arXiv:2211.12808 [nucl-th].
- [74] P. Haensel, A. Potekhin, and D. Yakovlev, Neutron Stars 1: Equation of State and Structure, Astrophysics and Space Science Library (Springer New York, 2006).
- [75] T.-T. Sun, Z.-Y. Zheng, H. Chen, G. F. Burgio, and H.-J. Schulze, Phys. Rev. D 103, 103003 (2021), arXiv:2101.07515 [nucl-th].
- [76] B. P. Abbott et al. (LIGO Scientific), Class. Quant. Grav. 34, 044001 (2017), arXiv:1607.08697 [astro-ph.IM].
- [77] M. Punturo et al., Class. Quant. Grav. 27, 194002 (2010).
- [78] O. E. Andersen, S. Zha, A. da Silva Schneider, A. Betranhandy, S. M. Couch, and E. P. O'Connor, Astrophys. J. 923, 201 (2021), arXiv:2106.09734 [astro-ph.HE].
- [79] B. Mueller, H.-T. Janka, and A. Marek, Astrophys. J. 766, 43 (2013), arXiv:1210.6984 [astro-ph.SR].
- [80] H. Sotani, T. Kuroda, T. Takiwaki, and K. Kotake, Phys. Rev. D 96, 063005 (2017), arXiv:1708.03738 [astroph.HE].
- [81] H. Andresen, E. Müller, H. T. Janka, A. Summa, K. Gill, and M. Zanolin, Mon. Not. Roy. Astron. Soc. 486, 2238– 2253 (2019), arXiv:1810.07638 [astro-ph.HE].
- [82] H. Andresen, B. Müller, E. Müller, and H.-T. Janka, Mon. Not. Roy. Astron. Soc. 468, 2032–2051 (2017), arXiv:1607.05199 [astro-ph.HE].
- [83] I. Bednarek, P. Haensel, J. Zdunik, M. Bejger, and R. Mańka, Astronomy & Astrophysics 543, A157 (2012).
- [84] N. Messios, D. B. Papadopoulos, and N. Stergioulas, Mon. Not. Roy. Astron. Soc. 328, 1161 (2001), arXiv:astro-ph/0105175.
- [85] C. J. Krüger, W. C. G. Ho, and N. Andersson, Phys. Rev. D 92, 063009 (2015), arXiv:1402.5656 [gr-qc].
- [86] H. Gholami, I. A. Rather, M. Hofmann, M. Buballa, and J. Schaffner-Bielich, Phys. Rev. D 111, 103034 (2025), arXiv:2411.04064 [hep-ph].
- [87] J.-E. Christian, I. A. Rather, H. Gholami, and M. Hof-mann, (2025), arXiv:2503.13626 [astro-ph.HE].